CHALMERS
UNIVERSITY OF TECHNOLOGY

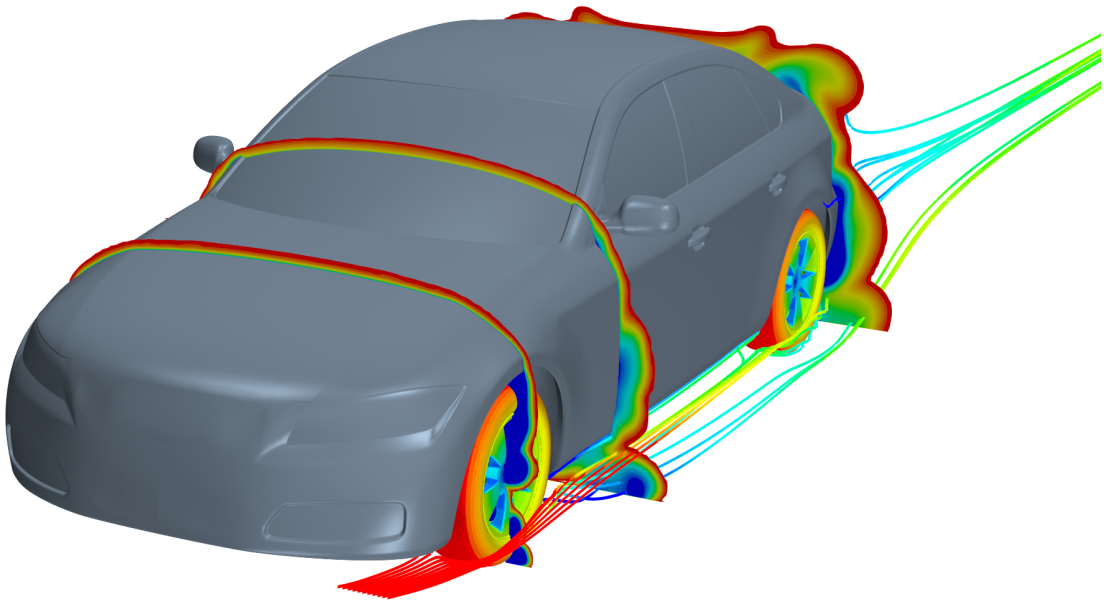

Aerodynamics Around Wheels and Wheelhouses

Master's thesis in Applied Mechanics

ÖMER FARUK CAVUSOGLU

Department of Applied Mechanics
CHALMERS UNIVERSITY OF TECHNOLOGY
Gothenburg, Sweden 2017

Master's thesis 2017:41

Aerodynamics Around Wheels and Wheelhouses

ÖMER FARUK CAVUSOGLU

CHALMERS
UNIVERSITY OF TECHNOLOGY

Department of Applied Mechanics
Division of Vehicle Engineering and Autonomus Systems
Chalmers University of Technology
Gothenburg, Sweden 2017

Aerodynamics Around Wheels and Wheelhouses
ÖMER FARUK CAVUSOGLU

Supervisor: Dr. Mohammad El-Alti, NEVS
Erik Zhong, NEVS
Examiner: Asst. Prof. Simone Sebben, Department of Applied Mechanics

Master's Thesis 2017:41
Department of Applied Mechanics
Division of Vehicle Engineering and Autonomus Systems
Chalmers University of Technology
SE-412 96 Gothenburg
Telephone +46 31 772 1000

Cover: Illustration of total pressure distributions in 3 different planes and streamlines around the wheels colored by total pressure.

Chalmers Reproservice Gothenburg, Sweden 2017

Aerodynamics Around Wheels and Wheelhouses
ÖMER FARUK CAVUSOGLU
Department of Applied Mechanics
Chalmers University of Technology

Abstract

The aerodynamic drag of an EV is the major energy consuming vehicle attributes, an EV requires less cooling flow, and can have a flat underbody, which potentially can improve the overall aerodynamics of the vehicle. The flow around the wheels and in the wheelhouses is a significant part of the total aerodynamic drag. Different aerodynamics concept vehicles have been studied in the past and shown in the automotive industry, the flow around wheels is managed and smoothen. They key for success is to manage the flow and keep the car functional and attractive. This master thesis project combines a through study of the historical and current aerodynamics concept cars regarding wheelhouse flows, comparing different rim designs, quantifying different features around the wheels or improvements in terms of drag reduction and range increase and finally a CFD study of DrivAer with implementing features/improvements.

Keywords: Wheel, EV , Drag reduction, Wheelhouse, Wheelhouse covered, Rim design, Aerodynamic drag, Deflector.

Acknowledgements

I would like to express my sincere appreciation to my supervisor,Dr. Mohammad EL Alti and Erik Zhong for their valuable guidance and support during the entire course of this study and for giving me a great opportunity to work at NEVS with such an interesting topic as Aerodynamics of wheels and wheelhouses. Thank you to my examiner Asst. Prof. Simone, discussions and feedback during the project. I would also like to express my gratitude to other engineers at aerodynamics department at NEVS for a wonderful atmosphere and productive discussions. In addition, thanks to Asst. Prof. Bayram Çelik for helping to come to Chalmers University of Technology and always supports me.
Special thanks go to my friend Ufuk Özcan whose expertise in the area of aerodynamic made a significant contribution to the project.
Lastly, but by no means least, I would like to thank my dear family, Hare Dursun, Nithin Syriac Kurien, Amy Liao, Berkan Işık and Talip Özturk for their constant support and encouraging during my thesis studies.

Thank you very much.

Ömer Faruk Cavusoglu,
Gothenburg, June 2017

Contents

List of Figures

List of Tables

1
Introduction

Car aerodynamics has become significant in the automotive industry development as it can crucially influence vehicle performance, comfort, safety, stability, cooling and visibility. Aerodynamic drag can be defined as the fluid drag force that occurs on a moving car with the direction of the fluid free stream flow. The total drag force occurs due to both the forces that produced by pressure distributions over the body surface and forces that are originating from skin friction [1].
Typically, 75-80 percent of the total driving resistance on today's cars occurs when the speed is at 80 km/h, coming from the aerodynamic drag force [2]. Figure 1.1 represents comparison between speed and resistance forces. Reducing power consumption is especially a vital aspect in electric vehicle (EV) design. NEVS plans to produce electrical cars in the near future and therefore aerodynamic design has been extremely important in order to design an efficient vehicle.

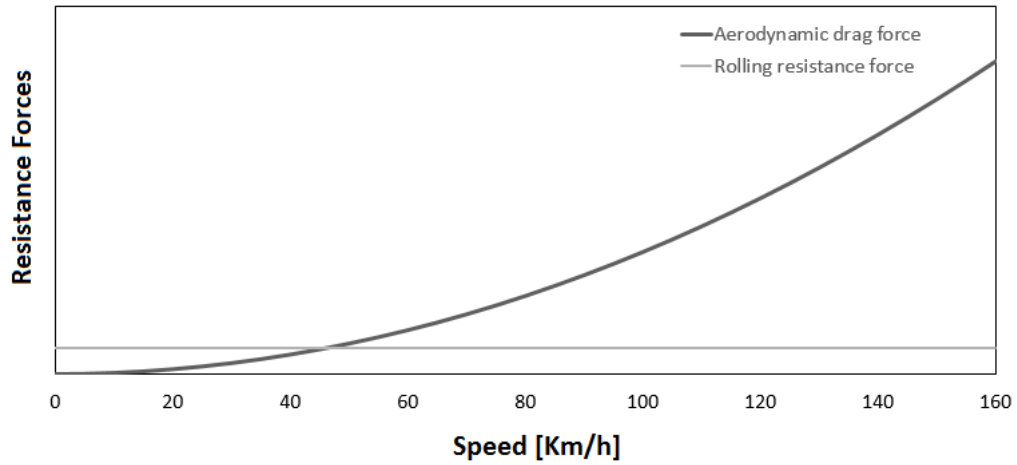

Figure 1.1: Comparing aerodynamic drag and rolling resistance.

The main objective of aerodynamic improvements on vehicles is to decrease drag. The best way for the drag reduction is focusing on the parts which create the largest percentage of the overall drag. Previous researches on the external bodies of cars have been simplified and achieved a considerable improvement from previous researches where the drag reduction attachments are also included in.
By now, most of aerodynamic researches include the shape of the upper body of vehicles. Figure 1.2 illustrates the drag ratios that occurs on different parts of a car. Nowadays, the upper body of a modern car determines about 45 % of the drag, while the bottom body determines 25 % (see. As for that wheels and wheelhouse flows

produce up to more than a quarter of the aerodynamic drag force [3]. An important part of this drag derives from the rotating wheels and the wakes they create. Furthermore, there are also important interaction results with the underbody flow and most significantly with base wake behind vehicle [4, 5, 6]. Reducing the drag that is caused by wheels and wheelhouses is an interesting solution to increase the range of car and to improve vehicle's road behavior. However, knowledge and prediction of underbody flow is quite restricted because of the complexity of the geometry [7, 8].

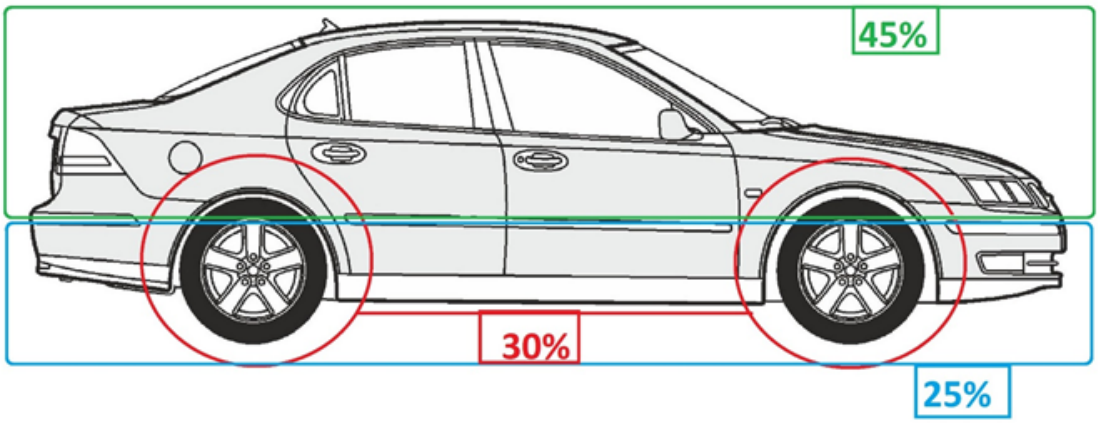

Figure 1.2: Relative contributions of vehicle sections to the overall drag coefficients for passenger vehicles [9].

Consequently the potential for further reduction in drag is through wheels and wheelhouses which provides the motivation for this research. In addition, requests for increasing EV's range, safety and the environment friendliness have driven aerodynamic researchers to improve the wheel and wheel housing of the vehicles for further potential improvements.
The main objective for this thesis is to investigate the aerodynamic effects of different heights on front wheel deflector, wheelhouse covers and different type of rim designs. Firstly, 5 different heighted front wheel deflector designs were used on the car. Secondly, 3 different configurations which are the front wheel-housing, the rear wheel-housing and both front and rear wheel-housing were covered. Thirdly, 7 different rim designs were used.

1.1 NEVS

National Electric Vehicle Sweden AB (NEVS) has been established as a Swedish company after the Saab Automobile bankrupted in 2012. NEVS provides services about electric vehicles and sustainable mobility. The company plans to provide electric cars and focus on mobility solutions for the future. NEVS as a trademark has been created to make this idea real.
NEVS recently decided not to use the SAAB name in their products. NEVS will have its own trademark for their own designs including the first electric vehicle in 2017 [10].

1.1.1 NEVS History

Properties of the Saab Automobile have been received by NEVS due to economic crises. The company made an agreement with Panda New Energy Co which is a Chinese vehicle leasing company that focuses on low emissions. NEVS has promised to produce 150,000 sedan electric cars to Panda till the end of 2020 [11]. NEVS also made a battery deal with Amperex in 2017 [12].

2
Theory

The concept of interaction between fluid and bodies is the most important part to figure out aerodynamics. Theory behind aerodynamics is pressure differences and skin friction , which can be described and applied with the Navier-Stokes equations. By the use of pressure and skin friction, drag can be calculated.

2.1 Governing equations

The equations that govern fluid flow are mathematical interpretations of the physical laws. These equations are known as the time dependent Navier-Stokes equations that consists of a continuity equation (2.1), a momentum equation (2.2), an energy balance (2.3) and a state equation, connecting density to pressure. If the fluid is assumed to be Newtonian the equations reduce to ,

$$\frac{\partial \rho}{\partial t} + \frac{\partial \rho u_i}{\partial t} = 0 \tag{2.1}$$

$$(\frac{\partial \rho u_i}{\partial t} + \frac{\partial \rho u_j u_i}{\partial x_j}) = \frac{\partial p}{\partial x_j} + \frac{\partial}{\partial t}(\mu(\frac{\partial u_i}{\partial x_j} + \frac{\partial u_j}{\partial x_i}) - \frac{2}{3}\mu\frac{\partial u_k}{\partial x_k}\delta_{i_j}) + \rho f_i \tag{2.2}$$

$$(\frac{\partial \rho E}{\partial t} + \frac{\partial \rho u_j E}{\partial x_j}) = -\frac{\partial p u_i}{\partial x_j} + \frac{\partial u_i \tau_{i_j}}{\partial x_j} + \frac{\partial}{\partial x_j}(k\frac{T}{x_j}) + S_E \tag{2.3}$$

In the above equations, f_i is an force applied on the fluid, S_E is an energy source term and the tensor $\tau_{i_j} = \mu(\frac{\partial u_i}{\partial x_j} + \frac{\partial u_j}{\partial x_i}) - \frac{2}{3}\mu\frac{\partial u_k}{\partial x_k}$. Equation of state relate pressure $p = p(\rho, T)$ internal energy $i = i(\rho, T)$ to the variables ρ and T. Thus allowing the above equations to be solved [13].

2.1.1 Incompressible fuids

At low Mach numbers (<0.3), compressible effects can be neglected ($\rho = cons$). As the continuity equation (2.1) reduces to

$$\frac{\partial u_j}{\partial x_j} = 0, \tag{2.4}$$

Equation 2.2 can be written for constant μ and incompressible flow [14].

$$\rho\frac{du_i}{dt} = \frac{\partial P}{\partial x_j} + \mu\frac{\partial^2 u_i}{\partial x_j \partial x_j} + \rho f_i \tag{2.5}$$

2.1.2 Boundary Layer

Walls are a source of vorticity in most flow problems of practical importance. Therefore, an accurate prediction of flow and turbulence parameters across the wall boundary layer is essential.The inner region of the boundary layer can be split up into three sublayers. In each of them the flow has different characteristics and can be modeled using different empirical approaches [15]. Very close to the wall is, what is usually called, the viscous sublayer where viscous damping reduce the tangential velocity fluctuations and normal velocity fluctuations are reduced by kinematic blocking [16]. The flow in this region is thus almost laminar. After the viscous sublayer comes the, so called, buffer layer and the fully turbulent log-law region, see Figure 2.1 Throughout these regions the turbulence is rapidly increased due to the increase in kinetic energy which is an effect of the large mean-velocity gradients [17].

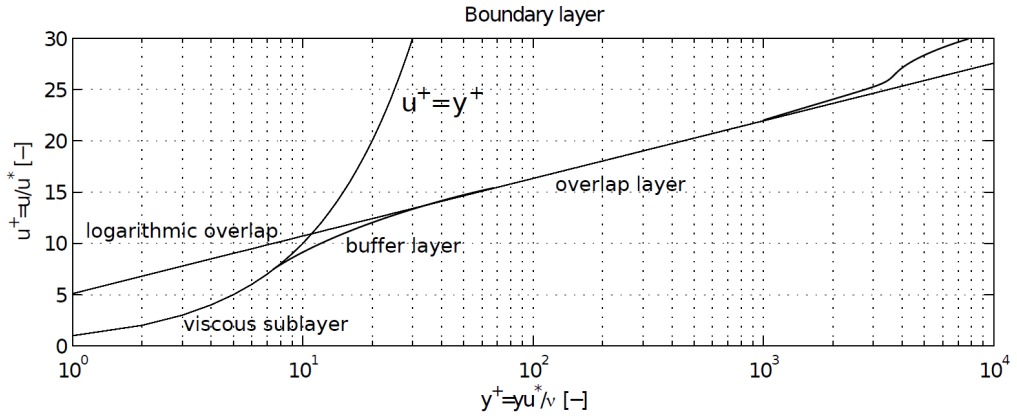

Figure 2.1: Velocity profile in the near wall region for a turbulent boundary layer

$$y+ = \frac{yu*}{\nu} \tag{2.6}$$

$$u* = 0.05U \tag{2.7}$$

Where u* is the friction velocity (Equation 2.7), ν is the kinematic viscosity and y is the height of the first cell [18].

2.2 Turbulence modelling

To solve the governing equations some simplications have to be made.

2.2.1 The Reynolds-averaged Navier–Stokes equations (RANS)

The Reynolds-averaged Navier–Stokes equations (or RANS equations) are time-averaged equations of motion for fluid flow. They are obtained from the instantaneous Navier-Stokes equations by the Reynolds Decomposition, called Reynolds

Average Navier Stokes (RANS). Approachment of RANS suggests that The instantaneous equations is split into its time-averaged and fluctuating quantities, Eq 2.8-2.11 [19].

$$p = \bar{p} + p' \tag{2.8}$$

$$u = \bar{u} + u' \tag{2.9}$$

$$v = \bar{v} + v' \tag{2.10}$$

$$w = \bar{w} + w' \tag{2.11}$$

Inserting the fluctuating quantities and time-averaging (Eq 2.12) into the Navier-Stokes equations;

$$\rho\bar{u_i}\frac{\partial\rho u_i}{\partial t} = \rho\bar{f_i} + \frac{\partial}{\partial x_j}[-\bar{p}\delta_{i_j} + 2\mu\bar{S_{i_j}} - \rho\overline{u_i'u_j'}] \tag{2.12}$$

there is an extra term in the time-averaged equation due to the fluctuations in turbulence, $\rho\overline{u_i'u_j'}$, which called the Reynolds stress tensor. So, at this point, for a 3-D flow, there are 10 unknowns; 4 from mean flow (p, u, v, w), and from turbulence ($\overline{uu}, \overline{uv}, \overline{uw}, \overline{vv}, \overline{vw}, \overline{ww}$) On the other hand, there are only 4 equations available (3 momentum + continuity); meaning that 6 more 10 equations are needed to close the system. This is the famous turbulence closure problem. Reynolds stress tensor can be modeled to solve this by an eddy viscosity and the velocity gradients. This approach is called as the Boussinesq assumption (Eq 2.13).

$$\rho\overline{u_i'u_j'} = \mu(t)(\frac{\partial\rho u_i}{\partial x_j} + \frac{\partial\rho u_j}{\partial x_i}) \tag{2.13}$$

δ_{i_j} is the Kronecker delta , k is the turbulent kınetic energy μt is the turbulent or eddy viscosity to be defined accordingly in different turbulence models.

2.2.2 k- ϵ model

This model is valid for fully turbulent flows only. A k-epsilon turbulence model consist of two-equation model that solves transport equations for the turbulent kinetic energy and its dissipation rate to determine the turbulent viscosity [15]. Widely used despite the known limitations of the model. Performs poorly for complex flows involving severe pressure gradients, separations and strong streamline curvature. Differential transport equations for the turbulence kinetic energy 2.2.2 and turbulence dissipation rate 2.15 [22].

$$\Big(\frac{\partial\rho k}{\partial t} + \frac{\partial\rho U_j k}{\partial x_j}\Big) = P_k - \rho\epsilon + P_{k_b} + \frac{\partial}{\partial x_j}\Big[(\mu + \frac{\partial\mu_t}{\partial\sigma_k})\frac{\partial k}{\partial x_j}\Big]$$

(2.14)

$$\Big(\frac{\partial \rho\epsilon}{\partial t} + \frac{\partial \rho U_j \epsilon}{\partial x_j}\Big) = \frac{\epsilon}{k}\Big(C_{\epsilon_1} P_k - C_{\epsilon_2}\rho\epsilon + C_{\epsilon_1} P_{\epsilon_b}\Big) + \frac{\partial}{\partial x_j}\Big[(\mu + \frac{\partial \mu_t}{\partial \sigma_\epsilon})\frac{\partial k}{\partial x_j}\Big] \tag{2.15}$$

$$\Big(\frac{\partial \rho k}{\partial t} + \frac{\partial \rho U_j k}{\partial x_i}\Big) = P_k - \beta * \rho\epsilon + P_{k_b} + \frac{\partial}{\partial x_j}\Big[(\mu + \frac{\partial \mu_t}{\partial \sigma_k})\frac{\partial k}{\partial x_j}\Big] \tag{2.16}$$

3

Methodology

The work presented in this paper is based on numerical computations.

3.1 Model preparation

CAD model obtained through NEVS in design department. In order to provide function properly in Star ccm+, CAD file should be prepared before volume mesh formed. ANSA program is used for cleaning up CAD file, creating purposefully and forminng surface mesh. Firstly vehicle's CAD file imported to ANSA. Since vehicle has symmetric form, it was bisected through x axis to simulate as a half car. Thus the total number of cells was halved. Consequently, both time for creating volume mesh and simulation time are reduced by half. All parts of vehicle named individually which provides convenience while making refinement at volume mesh. The problematic surfaces that may occur during importing or caused by CAD program was corrected.

Unnecessary small surfaces in the geometry were combined. Details assumed that wouldn't affects the result were ignored. Therefore, not only the size of CAD file decreased but also the numbers of volume mesh during creating volume mesh were prevented. Through cleanup processes, all errors were removed. Thus without the necessity of performing wrapper, finalized CAD was run in Star-CCM+ software impeccably. In Figure 3.1 , drivAer model before and after the Cleanup are shown.

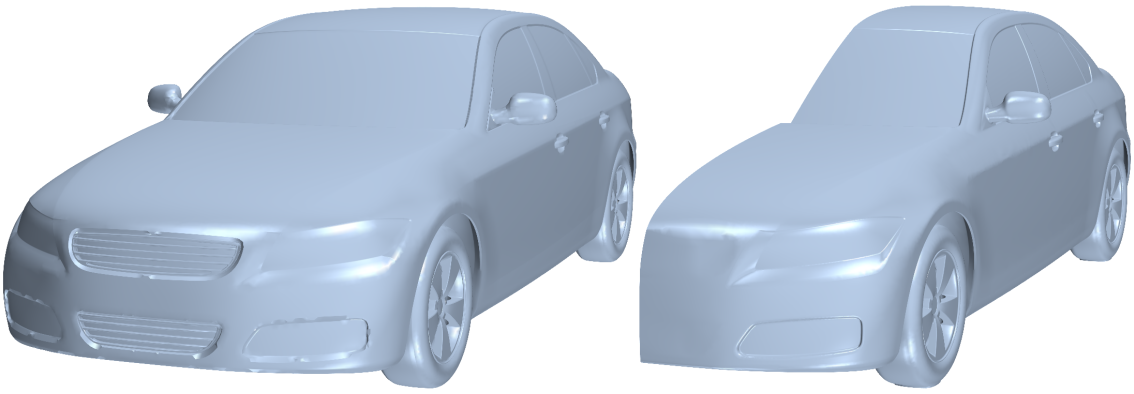

Figure 3.1: Before and after cleanup, DrivAer model.

3.2 Case description

The governing motivations for this study are to investigate the possibility to reduce the overall drag by implementing front wheel deflectors, enclosed wheel housing and tweaked rim design. In order to do that, several cases with different geometric setups must be done. The cases have been decided by previous studies about drag reduction [3, 17, 20, 21].

3.2.1 Front wheel deflector design

Front wheel deflector is fixed under the body in front of the wheel arch. 5 different configurations were simulated to find the most optimum deflector for reducing drag. The 5 different configurations were selected by changing the deflector height and keeping the width constant. The simulated deflector heights are in the range 20 mm to 50 mm in 10 mm increments. The deflector spans such that it starts at the same level of the side fender and goes up to the width of the tire. In Figure 3.2, the drivAer CAD-model with the front wheel deflector is shown.

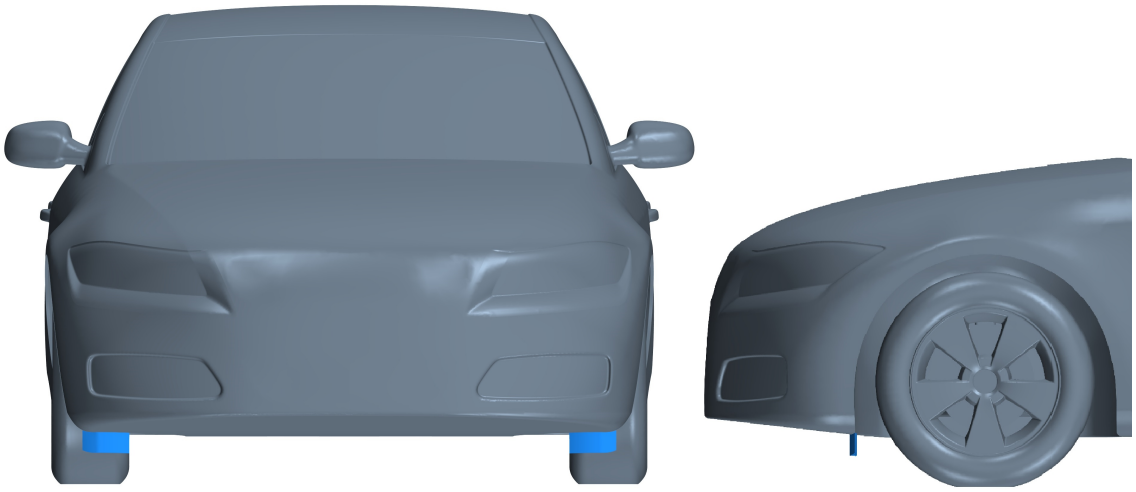

Figure 3.2: DrivAer Model with the front wheel deflector.

3.2.2 Wheelhouse design

In order to check the effect of aerodynamics on the partial and complete covering of the wheel arc, 3 configurations were simulated. The selected body designs of each case are shown in the Figure 3.3. The car body sections covering the wheel were designed such that there is a small protrusion to accommodate the wheels without friction.

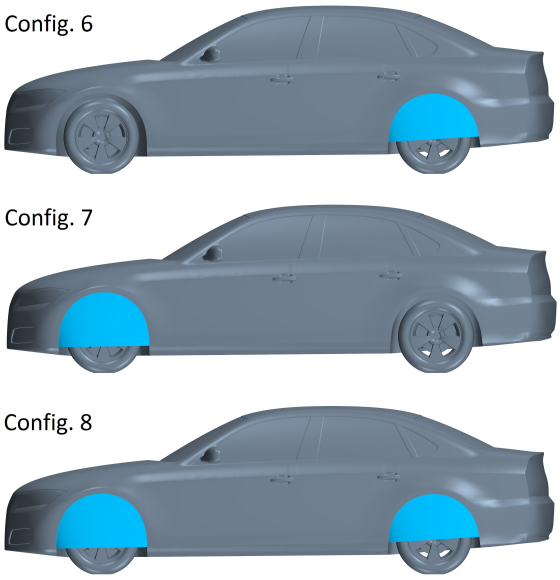

Figure 3.3: Configurations for wheel house covered.

3.2.3 Rim design

In this part of thesis, 7 different wheel configuration investigations have been performed to find optimum wheel design and to see effect on drag of car. The modifications from the Base model were shown in Figure 3.4. Last two rim configurations, used on NEVS 9-3, were supplied by NEVS.

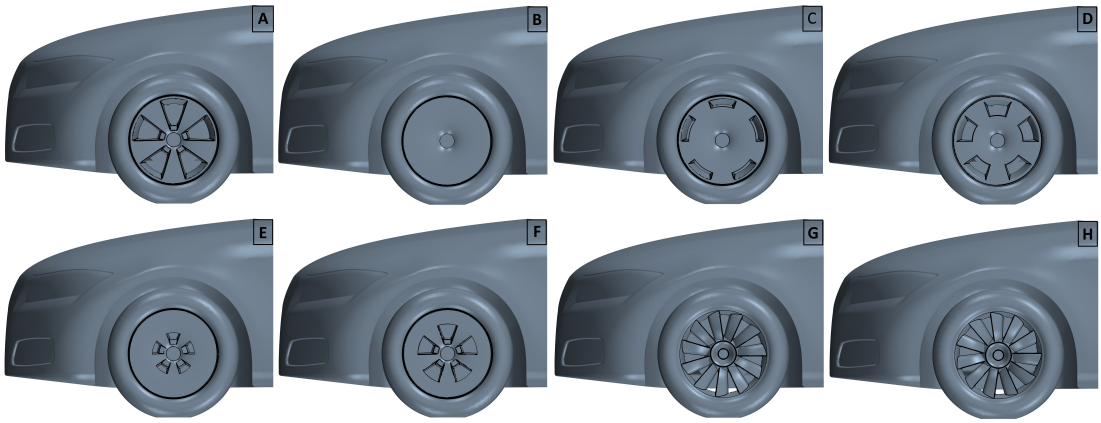

Figure 3.4: Rim design: (A) Base model, (B) Configuration 9,fully covered wheel, (C) Configuration 10, Inner wheel covered (40 mm gap thickness), (D) Configuration 11, Inner wheel covered (80 mm gap thickness), (E) Configuration 12, Outer wheel covered (40 mm gap thickness), (F) Configuration 13, Outer wheel covered (80 mm gap thickness), (G) Configuration 14, Fan type (H) Configuration 15, Mirrored fan type.

3.3 Case setup

3.3.1 Boundary condition

Star-CCM+ is used as solver for these simulations. A short description of the boundary conditions is presented in Table 3.1. A velocity inlet boundary condition prescribed a uniform velocity profile at 120 kph with turbulence intensity of 0.002 and Turbulent Viscosity Ratio of 200. At the outflow boundary, a pressure outlet boundary condition is specified a gauge pressure of zero. A slip boundary condition (symmetry) is specified on the tunnel walls to avoid the need to resolve the boundary layer on these surfaces.

Table 3.1: Boundary condition.

SURFACE/PART	MOVEMENT	TYPE	CONDITION
Tunnel-roof	stationary	symmetry	-
Tunnel-side	stationary	symmetry	-
Tunnel-symmetry	stationary	symmetry	-
Tunnel-floor	transitional x -velocity	wall	120 kph
Tunnel-inlet	stationary	Velocity-inlet	120 kph, 0^0 yaw Turb, Viscosity Ratio: 200 Turb, intensity: 0,002
Tunnel-outlet	stationary	Pressure-outlet	Gauge pressure: 0,0 [Pa] Turb, Viscosity Ratio: 200 Turb, intensity: 0,002
vehicle	stationary	Wall	No-slip
Wheels	Rotational velocity (y- axis)	Wall	No-slip 1015.82 RPM

3.3.2 Mesh generation

The computational mesh is created in STAR-CCM+ v11.06 which three types of volume mesher can be used to generate a volume mesh: Polyhedral, Tetrahedral and Trimmed Cell Mesher. In this thesis, Trimmed Cell Mesher is preferred. For both simple and complex mesh generation problems, the trimmed cell mesher provides a robust and efficient method of producing a high-quality mesh. The mesher model utilizes a template mesh that is constructed from hexahedral cells. Then the core mesh create the starting input surface is cut and trimmed. The mesh is made refinement that consider the local surface mesh size and local refinement controls. The prism layer mesh model is used with the volume mesh to generate orthogonal prismatic cells next to wall surfaces or boundaries.The prismatic layer is needed to predict the flow more accurate since the highest gradients are located near the wall.Finally, the Volume mesh is comprised mainly of hexahedral cells with trimmed cells and prism layers next to surface [15].
The numerical method used was a standard automotive CFD procedure based on guidelines from Star-CCM+ Guidelines. Half model which has a symmetric geometry was used as the case during simulation to reduce the number of mesh volumes.

It is created as a rectangular wind tunnel test section. It is approximately 3 vehicle lengths upstream the vehicle and 7 vehicle lengths downstream. The test section is around 10 vehicle widths wide and around 7 vehicle heights high. That gives a test section with the outer dimensions, 10 meters wide, 51 meters long and a height of 10 meters. The computational domain is illustrated in Figure 3.5.

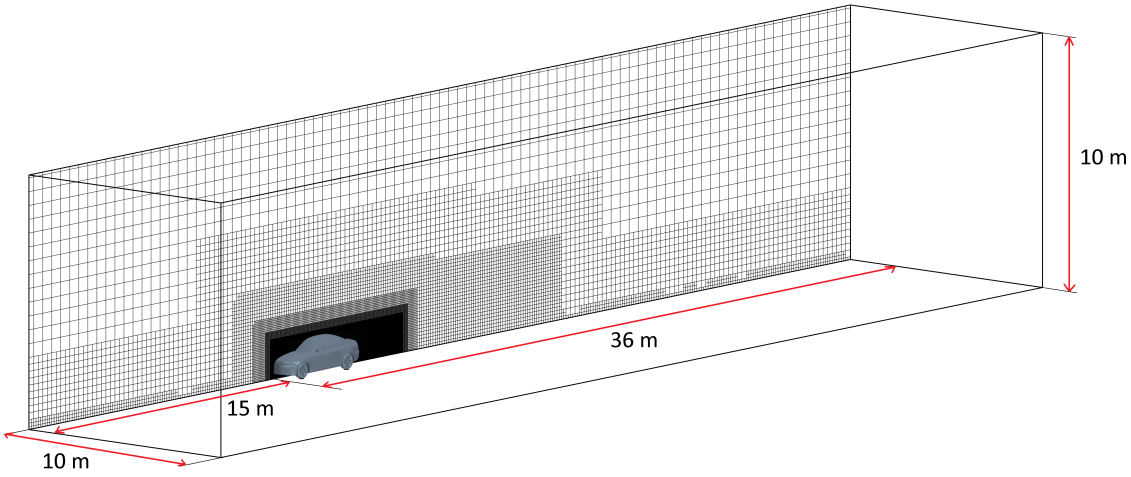

Figure 3.5: The domain.

The surface mesh of the vehicle has a resolution between 3 to 12mm. Since this is the main areas of interest in the study, the main focus and the highest resolution is of course in the vicinity of the wheels. On the vehicle body prismatic layer is used to reach lower than 5 y+ value, see Figure 3.6. The prismatic layer is needed to predict the flow more accurate since the highest gradients are located near the wall. In this study the number of layers has been set to between 12 and 8 with a geometric growth rate of 1.3.

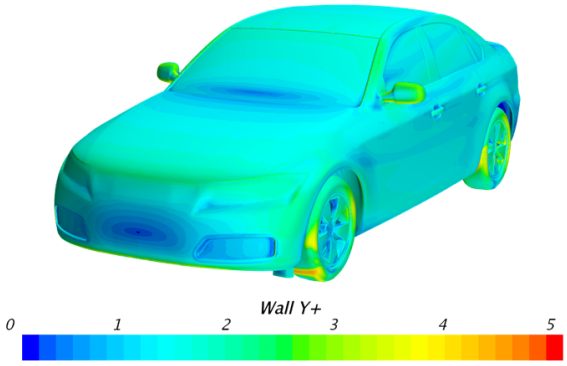

Figure 3.6: +Y value on the vehicle.

3.3.3 Mesh refinement

Alteration ratio of fluid properties differs according to calculation field's varied sections. In order to realize the changes, the mesh density should be increased where abrupt change occurs at fluid properties. For this reason high density meshing to

everywhere causes high calculating cost. So as to preclude this situation, points consist of rapid changes meshed more compact than the locations where the flow is more stable. Throughout regulating CAD File in ANSA, naming parts dissimilarly provides great convenience during mesh refinement. Zones, where sudden changes occurs at flow properties, which are body, side mirror, edges of body, rims, tires, disc hubs and disc prism layers are defined separately in the manner wall+ value smaller than 5. In this study the number of layers has been set to between 12 and 8 with a geometric growth rate of 1.3. 3 different refinement boxes is shown in Table 3.2.

Table 3.2: Refinement boxes.

Volumetric control	Percentage of Base	Absolute size
Refinement box 1	%600	150 mm
Refinement box 2	%300	75 mm
Refinement box 3	%80	20 mm

The bounding boxes used for the simulation can be seen from Figure 3.7. As can be seen form the Figure, the density of the mesh is the highest in the box closest to the vehicle. Figure 3.8 shows the close-up of the surface mesh of the Base model. Figure 3.9 shows the prism layer close to the walls of the vehicle, the height of the prism layer is smaller closer to the surface of the vehicle to calculate accurate C_D by providing Y+ value lower than 5.

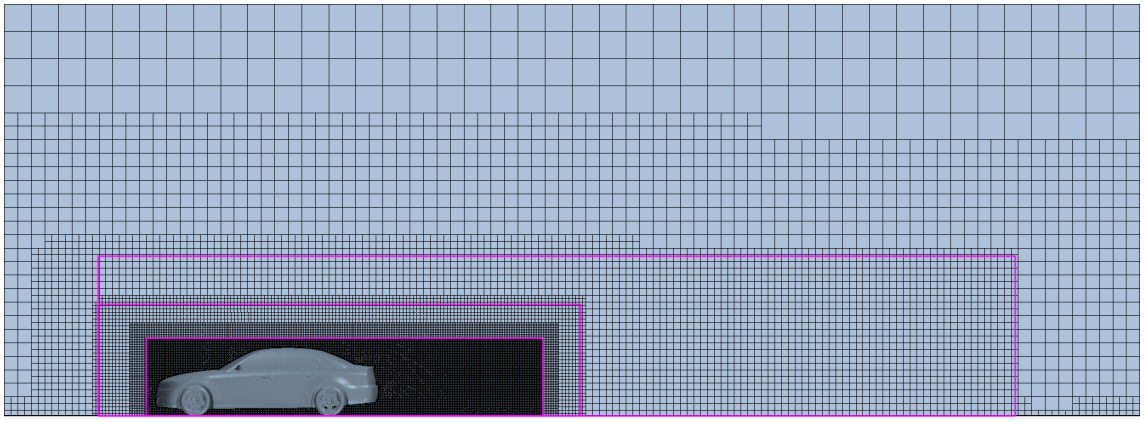

Figure 3.7: Refinement boxes around the vehicle.

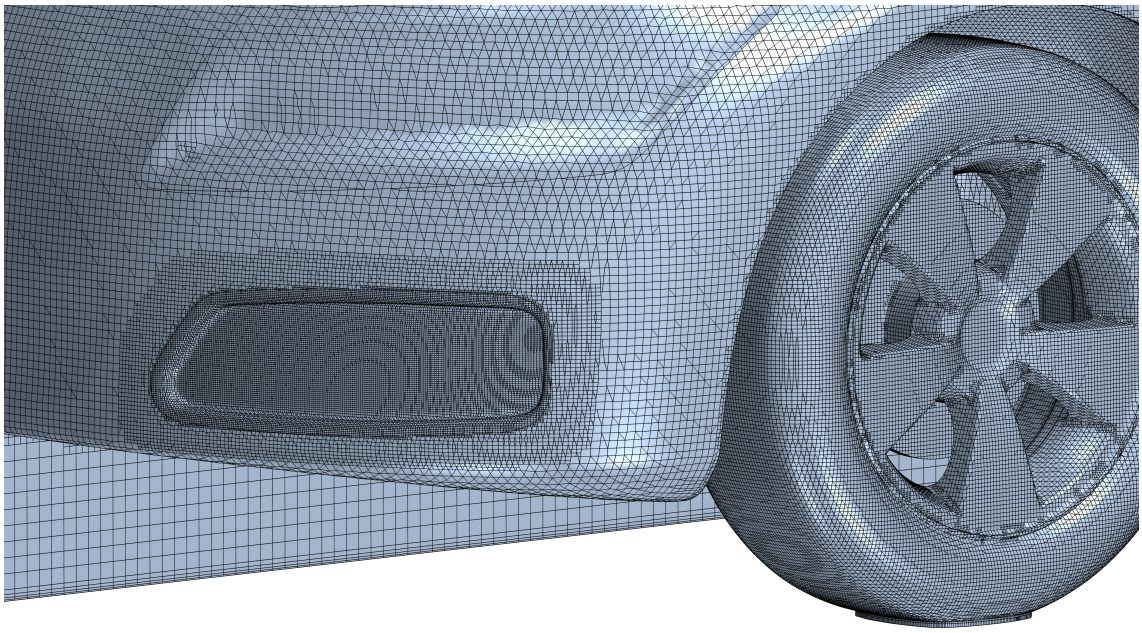

Figure 3.8: A close-up of the surface mesh of Base model.

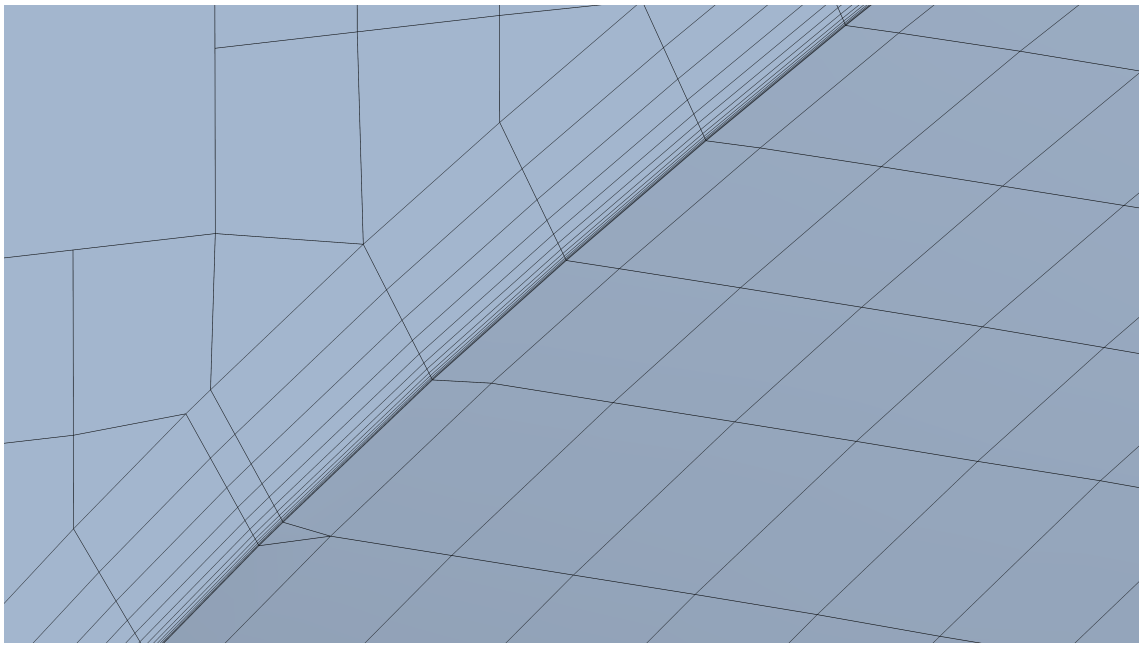

Figure 3.9: A close-up of the prism layers close to the walls of the vehicle.

4

Results

4.1 Accumulated body drag coefficient of Base model

Figure 4.1 shows the accumulated body drag coefficient along the longitudinal direction (X direction). Drag on a body is mainly caused by pressure and skin friction forces acting on the body. About 10 percent of the total drag on the body is due to skin friction. Accumulated drag coefficient caused by skin friction increases linearly along the longitudinal axis of the car. Since pressure forces are the main contributor to the drag on a body, the accumulated drag coefficient on the car shows nonlinearly changes along the body due to abruptly changes of surface pressure.
As seen in Figure 4.1 the accumulated drag coefficient changes suddenly around the front of the vehicle, windshield, rear window, wheel houses and back of the vehicle. The reason of these sudden changes is that the pressure drag originates from surfaces where the normal is x direction.

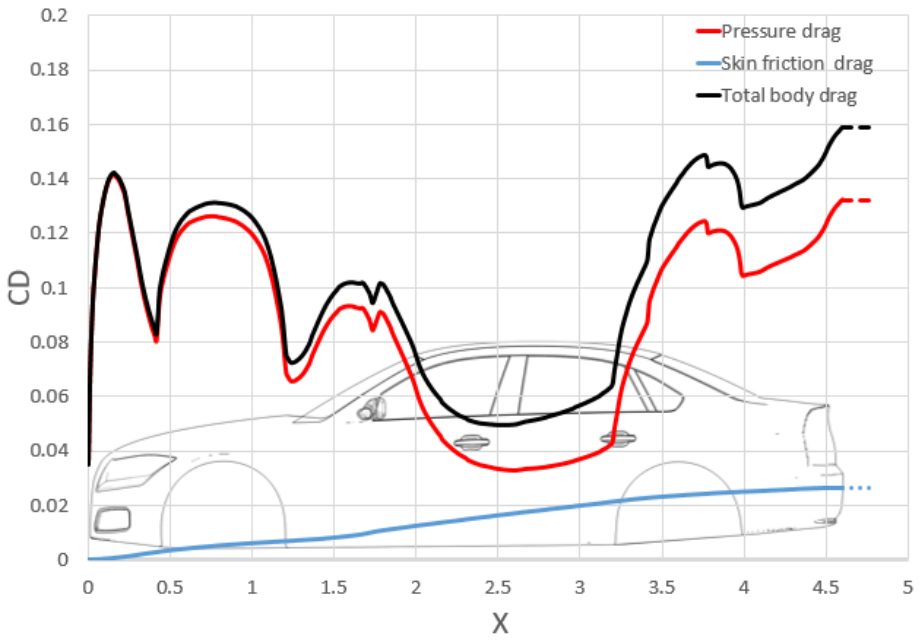

Figure 4.1: Accumulated Body C_D due to pressure and skin friction drag.

4.2 The influence of front wheel deflector height on car drag reduction

The aim of this part is to compare the influence of the front deflector height on the vehicle aerodynamic drag.

4.2.1 Drag comparison

We have considered deflectors with constant width and changed the height as follow 20, 30, 40, 50, 60 mm. The vehicle C_D with the front deflectors of different heights are shown in Table 4.1. As seen from the table the C_D value of the front wheel decreases while deflector height increases. The total drag of vehicle decreases with the increasing deflector height until an optimum height (40 mm). Further increase of the deflector height increases the drag. Max decrement in the C_D value is around 5.5 % with the deflector height of 40 mm. Deflectors with more than 40 mm height have higher drag compared to the deflector with 40 mm, but still lower than the Base model.

Table 4.1: C_D change with front wheel deflector height.

Model	Front wheel deflector heights (mm)	Total Cd	Body Cd	Front Wheel Cd	Rear wheel Cd	Cd of Deflector
Base model	-	0,216	0,159	0,031	0,022	0
Configuration 1	20	0,210 (-%2,78)	0,152	0,029	0,024	0,002
Configuration 2	30	0,208 (-%3,70)	0,151	0,027	0,025	0,004
Configuration 3	40	0,204 (-%5,55)	0,148	0,025	0,025	0,005
Configuration 4	50	0,204 (-%4,17)	0,150	0,025	0,024	0,006
Configuration 5	60	0,215 (-%0,46)	0,165	0,023	0,02	0,007

4.2.2 The front wheel comparison

Since the deflector reduces the area of the front wheel exposed directly to upstream, the drag coefficient of the wheel reduces as the height of the deflector increases. As seen from Table 4.1, the decrease of the front wheel drag coefficient is proportional to the increase of the drag coefficient on the deflector. The pressure coefficient distribution on the front wheel is shown in Figure 4.2. The high pressure region is decreased with increasing deflector height. The velocity field on near ground surface for The Base model and Configuration 3 are shown in Figure 4.3. Simulation results show that the deflector doesn't only effect C_D value of front wheel but also reduces the under body mass flow rate. The main reason of this reduction is changing the direction of the flow that was toward front wheel.

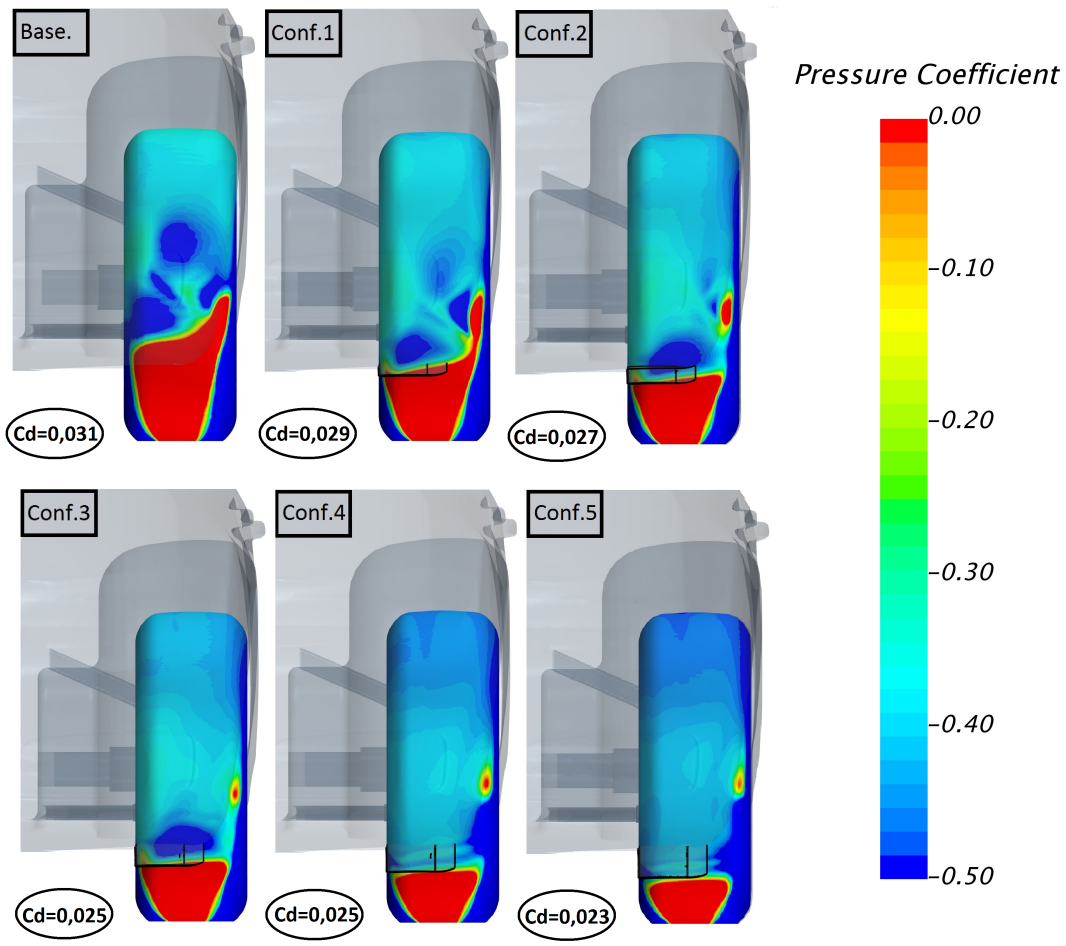

Figure 4.2: The C_D distribution of front wheel surface in front view .

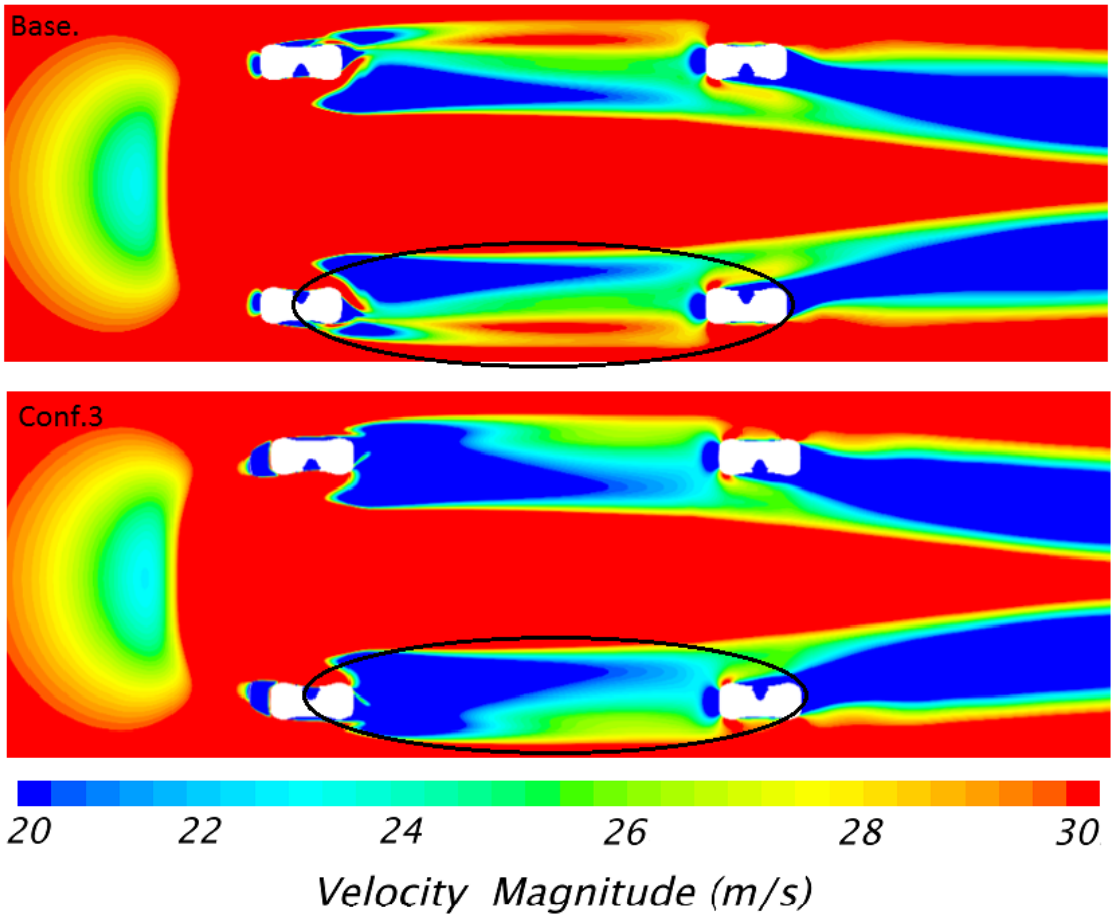

Figure 4.3: The velocity field on near ground surface for the base model and Configuration 3.

4.2.3 Body drag

Figure 4.4 shows accumulated body drag coefficient difference between Configuration 3 and Base model. Only the accumulated drag on Configuration 3, which gives minimum body drag coefficient value, was considered to show the effects of deflector on the body. It can be clearly seen that the deflector effect on drag differs on each part of the vehicle. These differences are mainly due to before mentioned effects of deflector on under body flow. It can be seen that the front wheel deflector gives an initial drag increment on the body compared to the base model. Significant drag increase occurs at the upstream of the front wheel center compared to the Base model, after the center the drag starts to reduce and continues to decrease until the end of the wheelhouse. Cumulative drag of Configuration 3 is about 8 count less than Base model at the end of the wheelhouse. The drag difference does not change considerably until the rear wheel, then decreases up to the center, and then increases until the end of the rear wheel. Due to increase of the back pressure the drag decreases suddenly at the back of the car. It results in the overall body drag reduction of around 11 count compared to the reference.

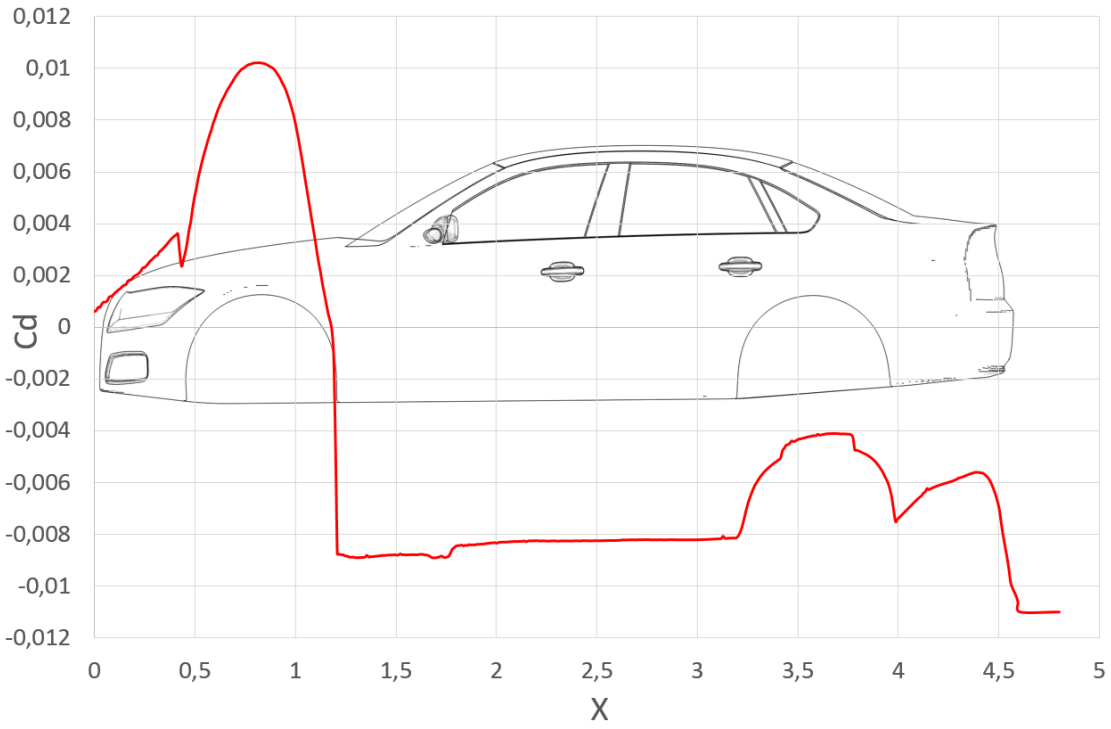

Figure 4.4: The accumulated body drag coefficient difference between Configuration 3 and Base model.

Total pressure contour is used to show the change of flow energy and velocity vector diagram is used to show characteristic of flow at current zone. Thereby the characteristic of flow at wheelhouse is expressed. As seen in Figure 4.5 - 4.8, after adding front deflector, separation point position is lowered. As it is understood from velocity vectors, vortex occurs in the separation region in front of the wheel. For this reason flow energy consumption increase. Behind the deflector, total pressures de-

creases depending on deflector's height. This decline of the pressure causes a sudden increment of drag.

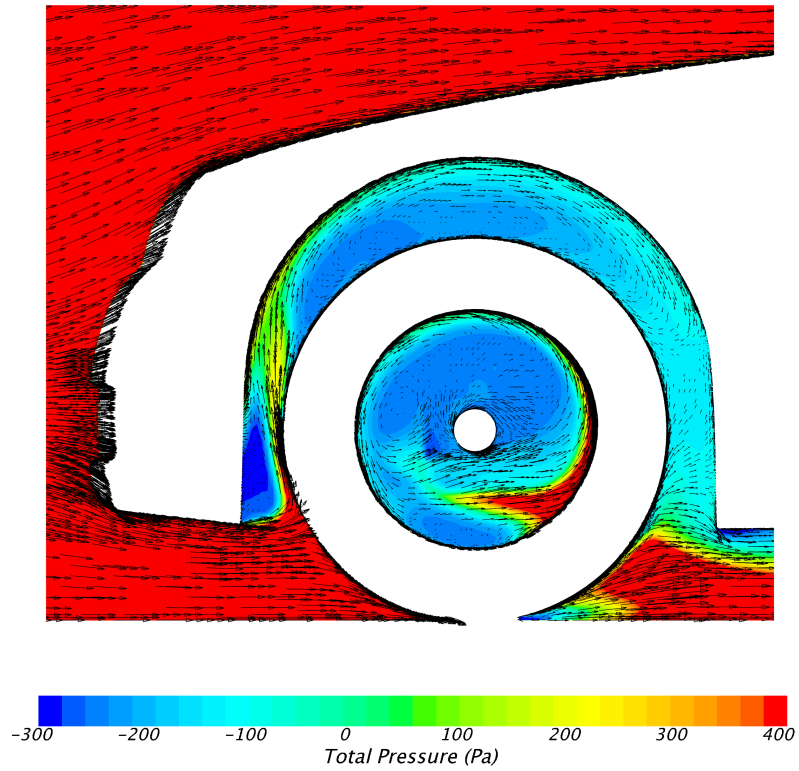

Figure 4.5: Total pressure contour and velocity vector diagram of front wheel center symmetry plane for Base model.

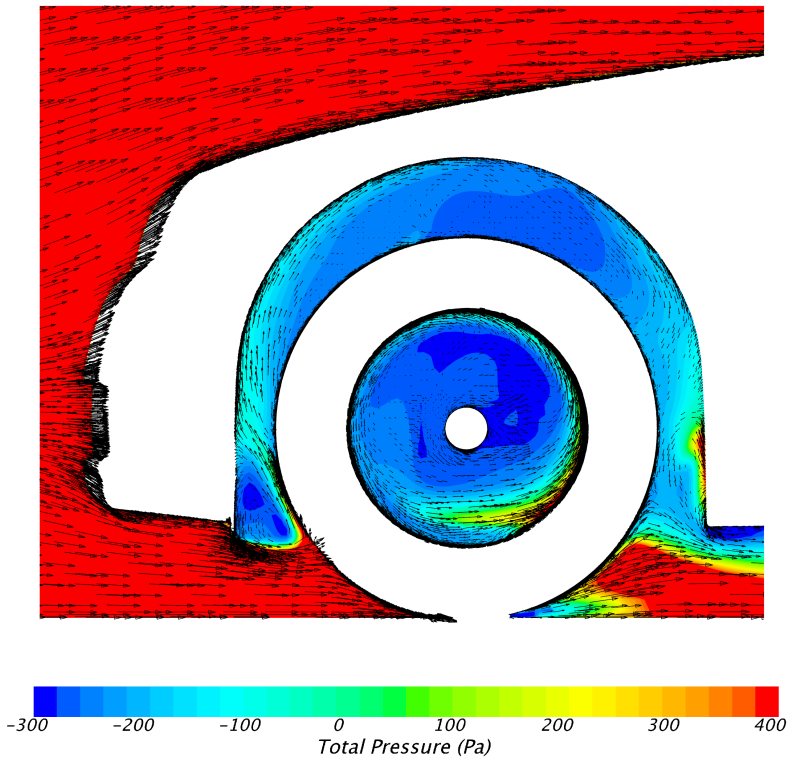

Figure 4.6: Total pressure contour and velocity vector diagram of front wheel center symmetry plane for Configuration 1.

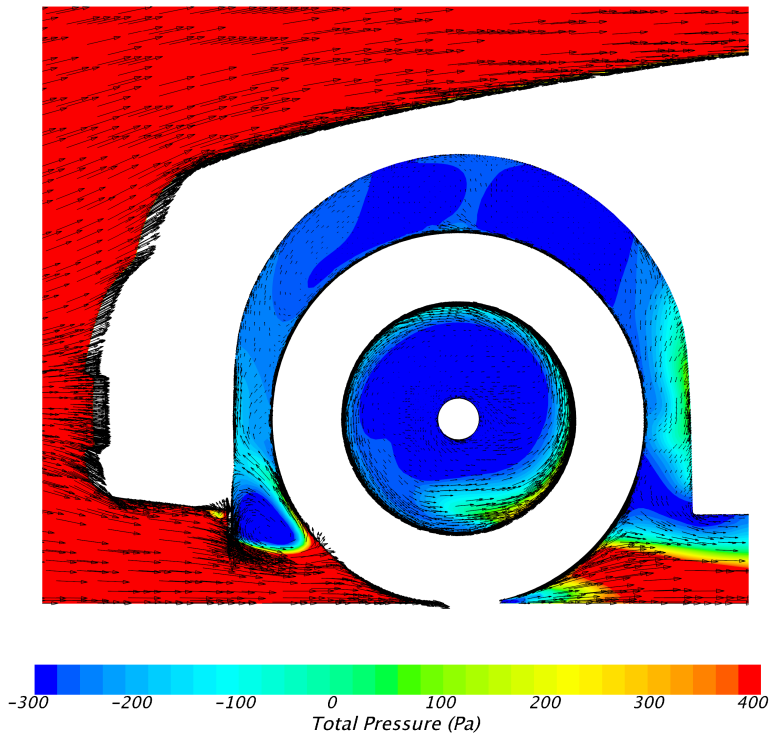

Figure 4.7: Total pressure contour and velocity vector diagram of front wheel center symmetry plane for Configuration 3.

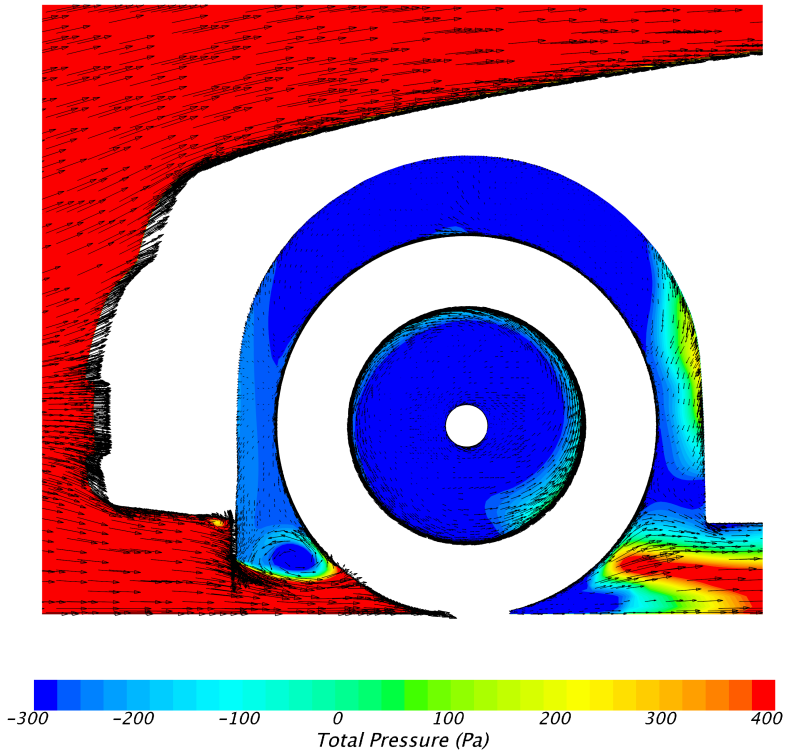

Figure 4.8: Total pressure contour and velocity vector diagram of front wheel center symmetry plane for Configuration 5.

Another important effect of the deflector is the change in pressure at the back of the car. As seen in Figures 4.9 - 4.12, the base wake for the vehicle can be seen from the velocity magnitude in x-y plane of the wheel center. Low velocity field at vehicle rear end is rather large at Base model. Hence, as wake is large at Base model, it can be inferred that back pressure is low. It's clear from Configuration 1 (with 20mm deflector) low velocity field decreases or separation is deferred. Base wake of Configuration 3 is slightly narrower than Configuration 1. So it means that back pressure of Configuration 3 is higher than Configuration 1. In Configuration 5 (with 60mm deflector) low velocity field increases correspondingly back pressure decreases. As mentioned before, the deflector alters under body flow, which affects the flow in the wake of the car, which in turn changes the pressure on the back of the car. In short, with increasing the height of deflector, first the pressure on the back of the car increases, after 40 mm deflector height (Configuration 3) the pressure starts to decrease as shown in Figures 4.13 - 4.16.

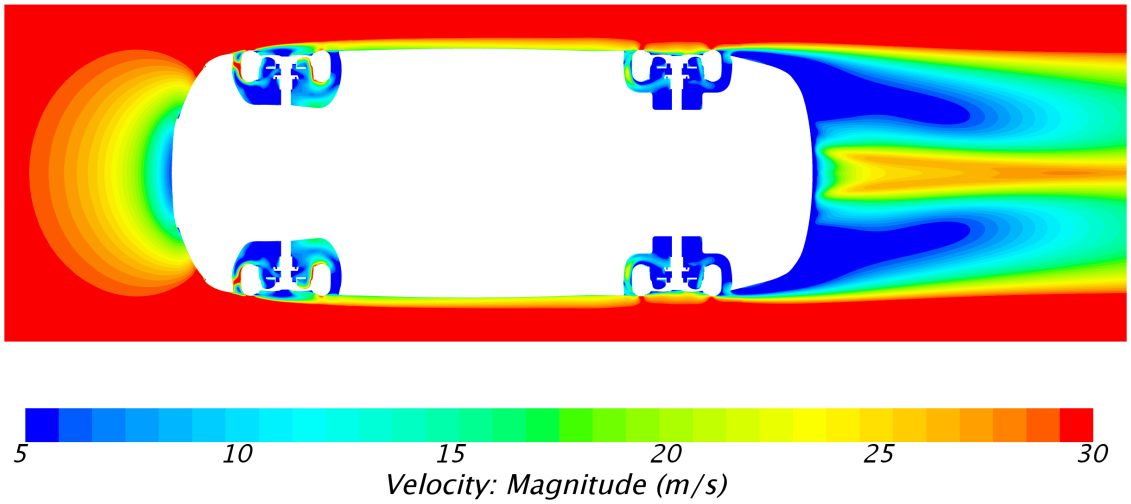

Figure 4.9: Velocity magnitude in x-y plane of the wheel center for Base model.

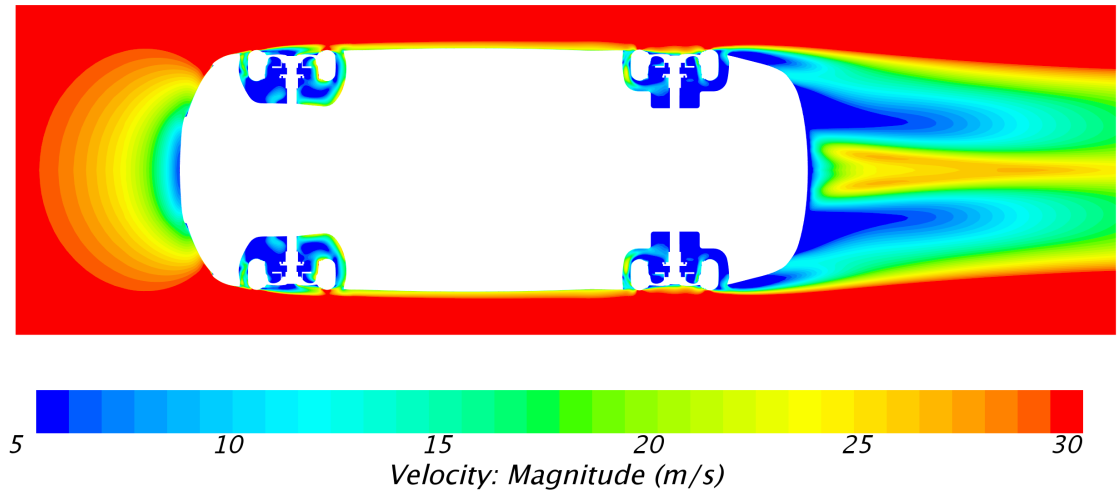

Figure 4.10: Velocity magnitude in x-y plane of the wheel center for Configuration 1.

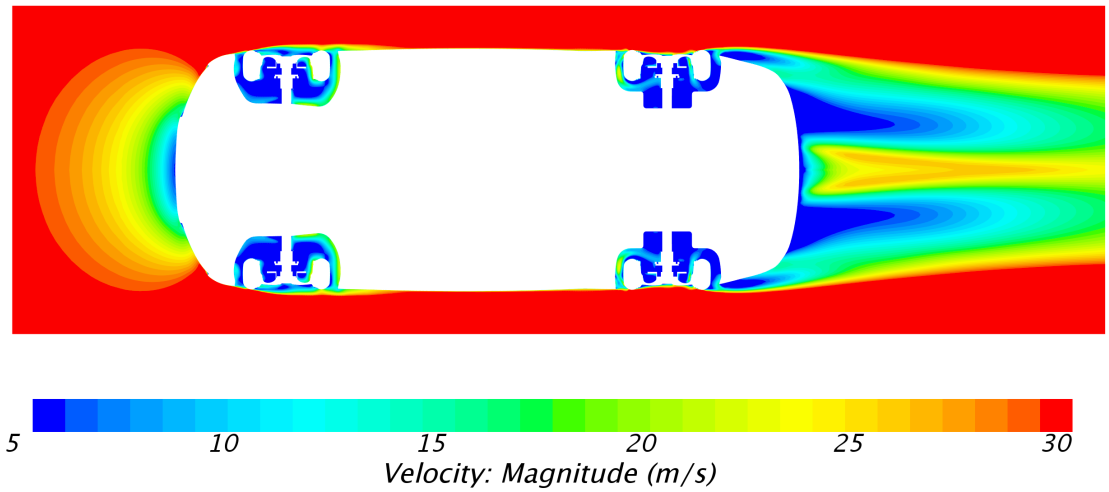

Figure 4.11: Velocity magnitude in x-y plane of the wheel center for Configuration 3

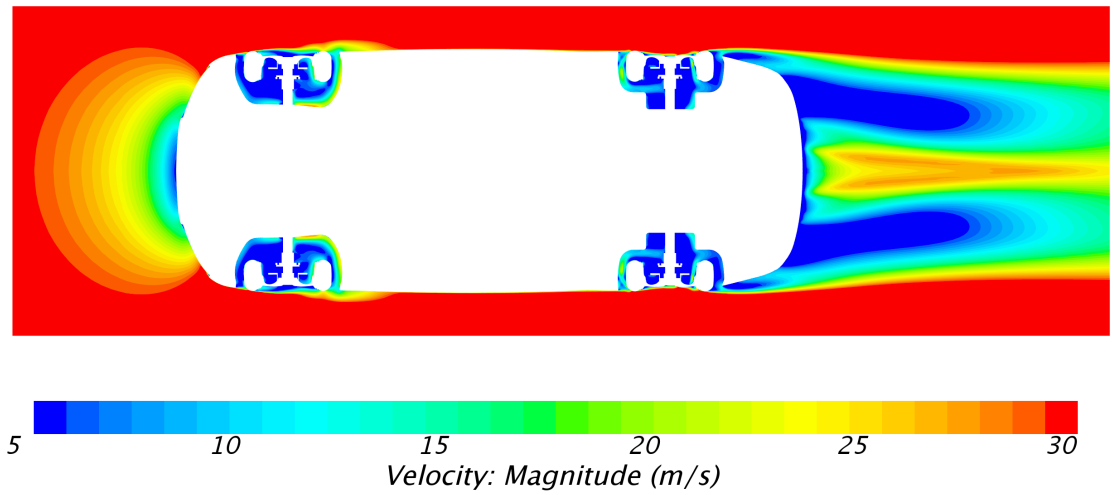

Figure 4.12: Velocity magnitude in x-y plane of the wheel center for Configuration 5.

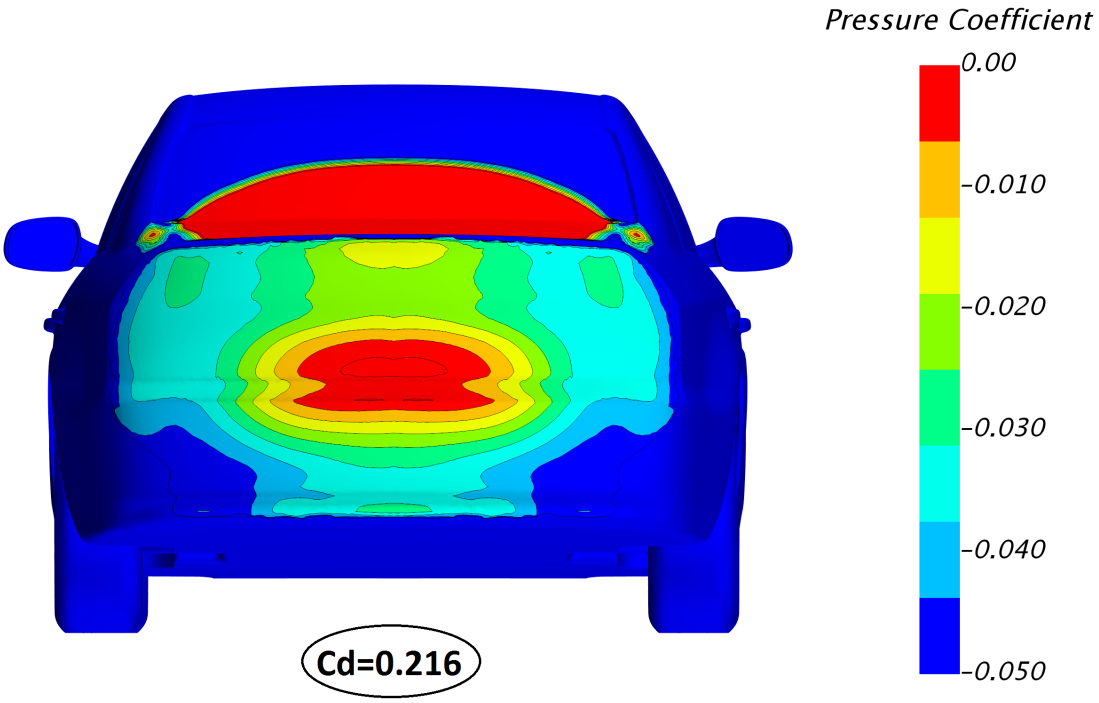

Figure 4.13: Back pressure measurements for Base model.

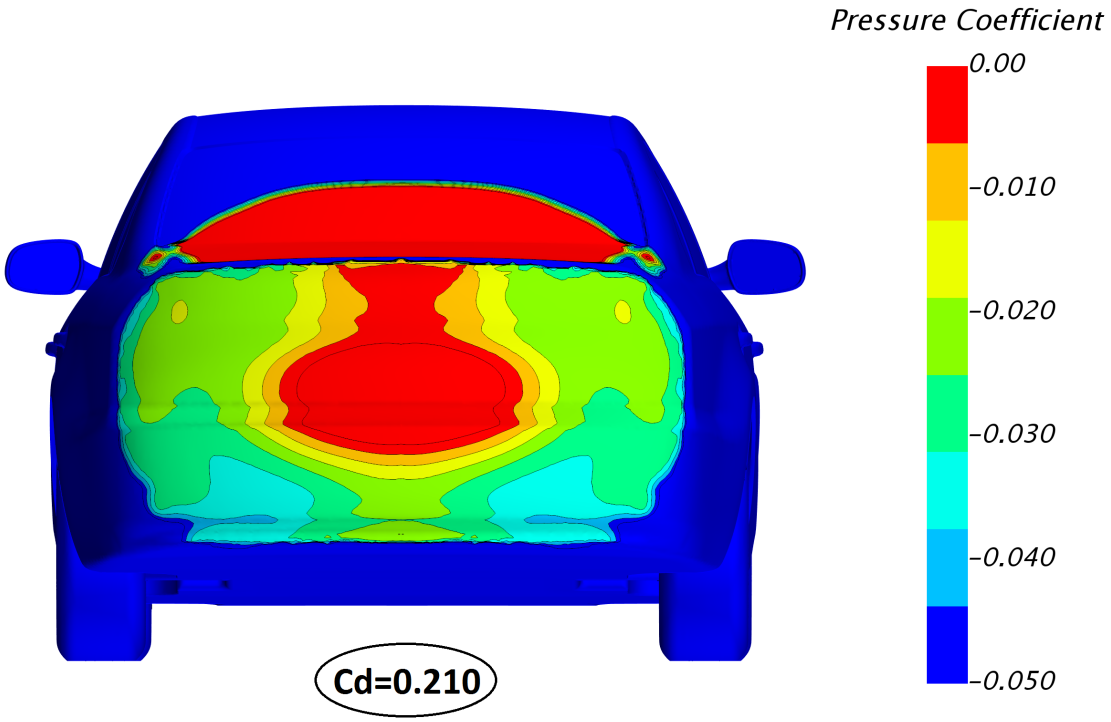

Figure 4.14: Back pressure measurements for Configuration 1.

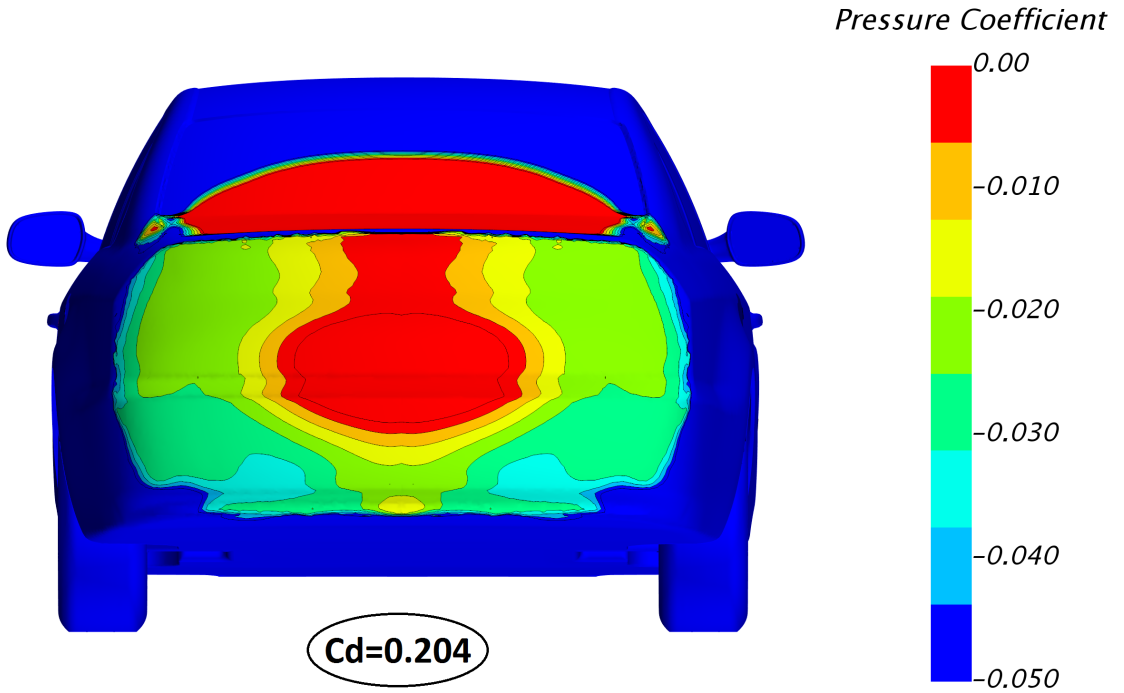

Figure 4.15: Back pressure measurements for Configuration 3.

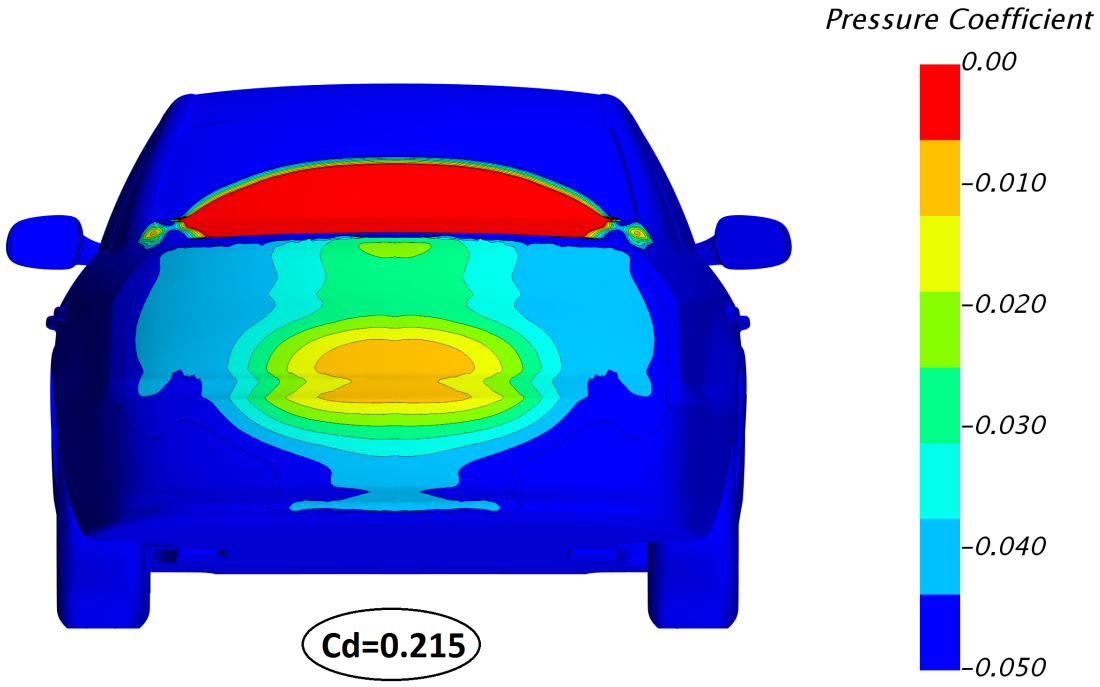

Figure 4.16: Back pressure measurements for Configuration 5.

4.3 The influence of wheelhouse cover on car

4.3.1 Drag comparison

Aerodynamic drag coefficients of Base model and Configurations 6 to 8 are shown in Table 4.2. As seen from the table the drag coefficient decreased on each Configuration comparing to Base model. Since wheelhouse cover changes front area of the vehicle, C_D *A's of configurations were considered. Additionally, C_D and C_D*A difference between configurations and Base model are shown as percentage to realize effect of different frontal area.

Table 4.2: C_D and $C_D * A$ for Base model and Configuration 6-8

Configurations	Cd	Difference of Cd	Cd*A	Difference of Cd*A
Base model	0,216	-	0,233	-
Configuration 6 (Rear wheel arch covered)	0,210	-0,0062 (-2,9%)	0,228	-0,0054 (-2,3%)
Configuration 7 (front wheel arch covered)	0,207	-0,0091(-4,2%)	0,224	-0,0093 (-4,0%)
Configuration 8 (both wheel arch covered)	0,208	-0,0081 (-3,8%)	0,226	-0,0073 (-3,1%)

Aerodynamic body drag coefficients of Base model and Configuration 6 to 8 are shown in Table 4.3. It can be inferred from Table 4.3 that body C_D of Configuration 7 which gives minimum drag value, almost didn't change but when overall car is considered, C_D and C_D*A reduction is equal to 9 count. In other words, most of the reduction originates from other part of the car, wheels, hubs and discs. Since the drag coefficients of hubs and discs are not significant, their effects aren't given in the table.

Table 4.3: Body C_D and $C_D * A$ for Base model and Configuration 6-8

Configurations	Cd	Difference of Cd	CdA	Difference of CdA (%)
Base model	0,159	-	0,171	-
Configuration 6	0,155	-0,0038(-2,4%)	0,168	-0,0033 (-1,9%)
Configuration 7	0,158	-0,0016(-1,0%)	0,170	-0,0013 (-0,8%)
Configuration 8	0,160	+0,0010(+0,6%)	0,173	+0,0020 (+1,1%)

CD of wheels for Base model and Configuration 6-8 are given Table 4.4 the drag coefficient for the front wheel of Configuration 6 where rear wheel arch is covered

is the same value as Base model, the C_D of the rear wheel decrease 5 count. C_D of front wheel decrease 5 counts as to rear wheel's decrease 2 counts at Configuration 7 with covered front wheel arch. As for Configuration 8 with both front and rear wheel arches covered, while C_D of front wheel and rear wheel decrease 5 and 7 counts, respectively. Although the largest decline of the total wheel's drag coefficient occurred at Configuration 8, the decrease in the value of total drag coefficient is the most at Configuration-7, due to the increase on the body drag of Configuration 8.

Table 4.4: C_D of wheels for Base model and Configuration 6-8 .

Configurations	Front wheel Cd	Rear wheel Cd	Front and rear wheels total cd
Base model	0,031	0,022	0,053
Configuration 6	0,031	0,017	0,048 (-0,005)
Configuration 7	0,026	0,020	0,46 (-0,007)
Configuration 8	0,026	0,015	0,41 (-0,012)

4.3.2 Body drag

In Figure 4.17, body accumulated C_D difference between Base model and 3 different configurations (Configuration 6,7 and 8) are shown. Since only rear wheel arch is closed at Configuration-6, accumulated drag difference between Base Model and Configuration-6 is almost same up to rear housing. Then, drag increased from front of the rear wheel house to center of the wheel and decreased until end of the wheel house. Then on the back, C_D value decreased almost 8 counts. due to the rear wheelhouse cover, overall body C_D of Configuration 6 decreased 6 counts.
Between front of car (x=0) and front of the wheelhouse, the difference is almost constant at Configuration-7 while drag coefficient decreased at front wheel house because of front wheel cover. There is no significant change occurred until the end of the rear wheel house. At last, drag difference decreased sharply at back of the car. Accumulated drag of Configuration 8 is similar with Configuration 7 up to the rear wheel house. Drag coefficient decreased at rear wheel house compared to Configuration 7. At the end of the car, accumulated drag is more than Base model.

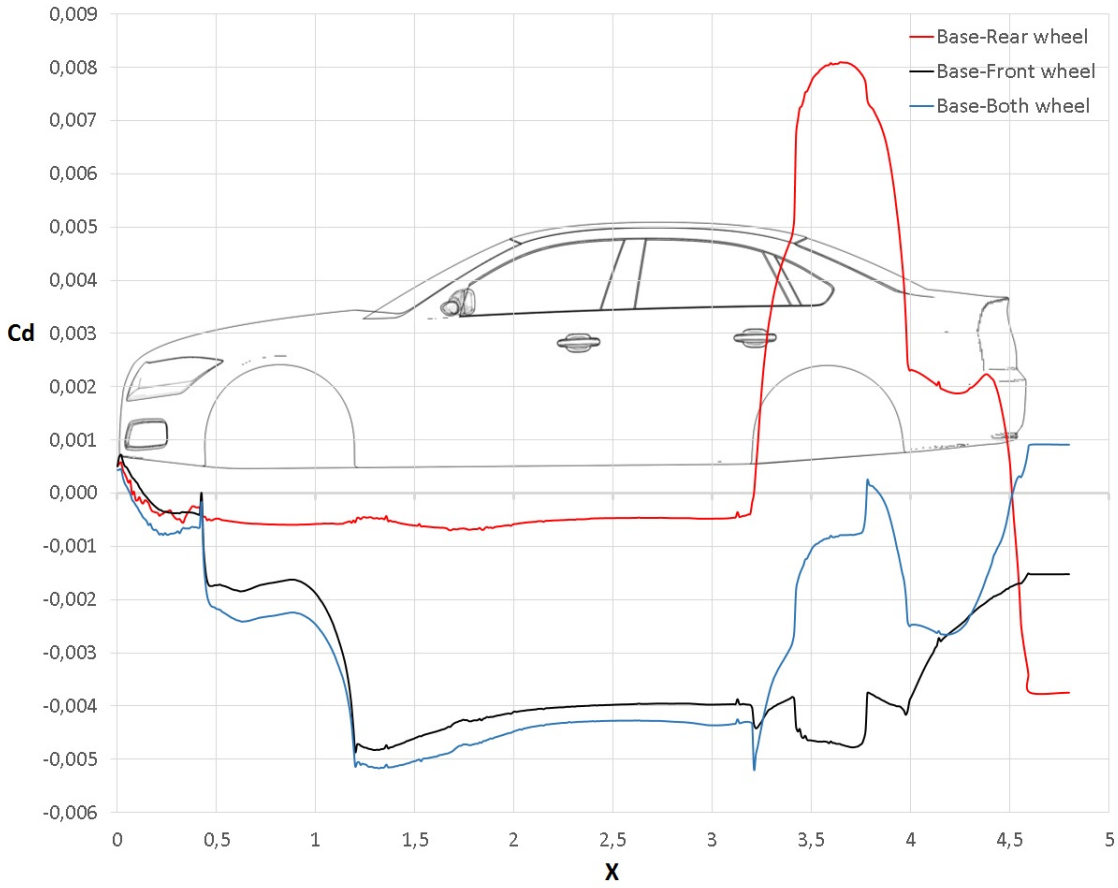

Figure 4.17: Body accumulated C_D difference between Base model and 3 Configuration (Configuration 6,7 and 8)

In Figure 4.18, C_P distributions in back of front wheelhouse are shown. It is clear that in Configuration 6, the drag coefficient does not change in that area. However, on Configuration 7 - 8, the C_P decreases so drag also decreases in that area

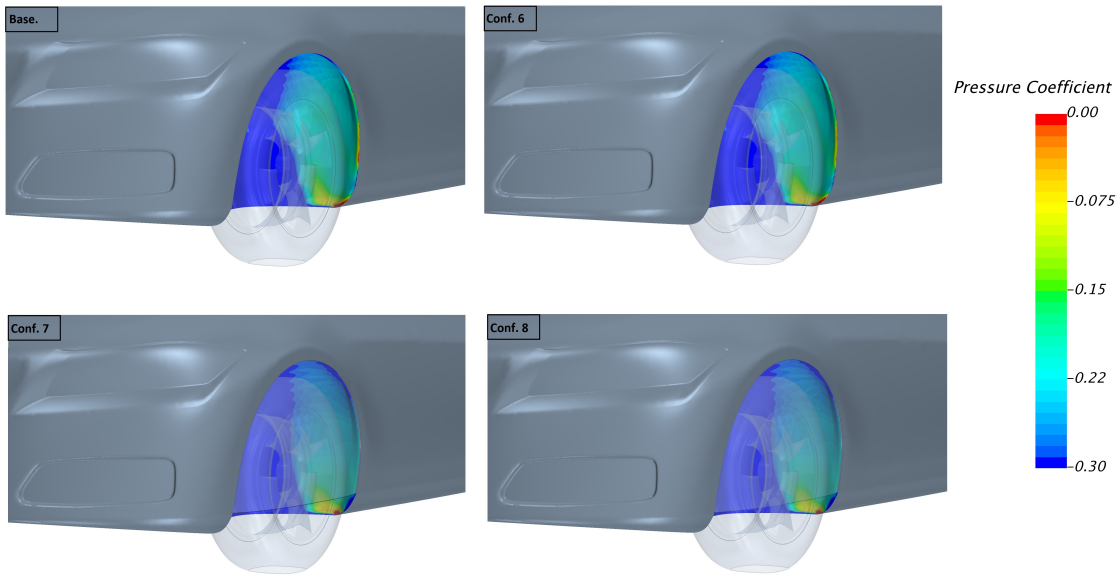

Figure 4.18: Pressure coefficient distributions in rear of front wheels

As mentioned before (see Table 4.3), when only considering body of vehicle, the most drag coefficient reduction is on Configuration 6. Also as seen Figure 4.19, on Configuration 6, high pressure area increased comparing to Base model. However, there is no remarkable difference in back pressures between base model and Configuration 7- 8. Their back pressure contours appearances are virtually same as Base model.

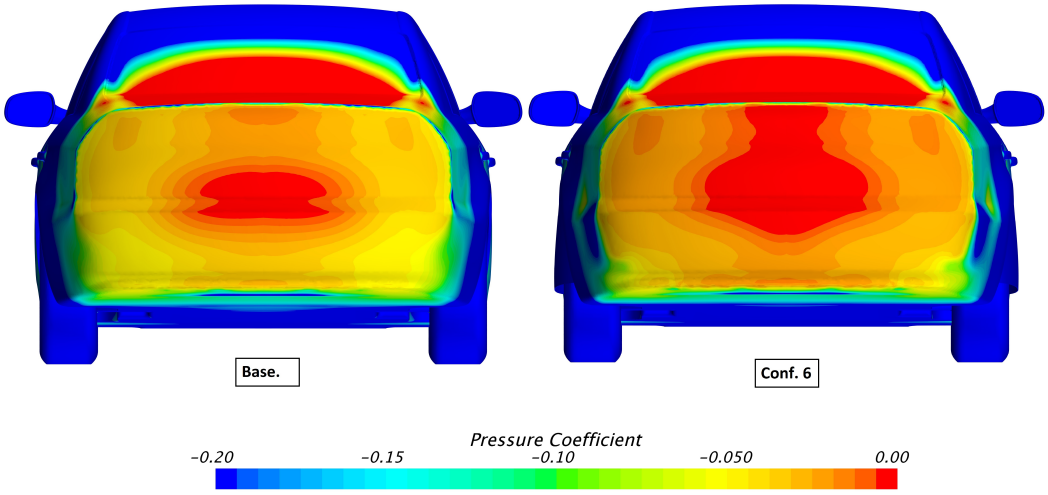

Figure 4.19: Back pressure of Base model and Configuration 6

In Figure 4.20, it can be seen that separation occurs behind the rear wheel house. This separation interacts with the base wake changing both its size and shape. The separation behind the rear wheels at Configuration 6 is narrower due to the rear wheel housing. Due to smaller the separation, at Configuration 6, base wake is

smaller and narrower which means higher back pressure and drag reduction (see Figure 4.21).

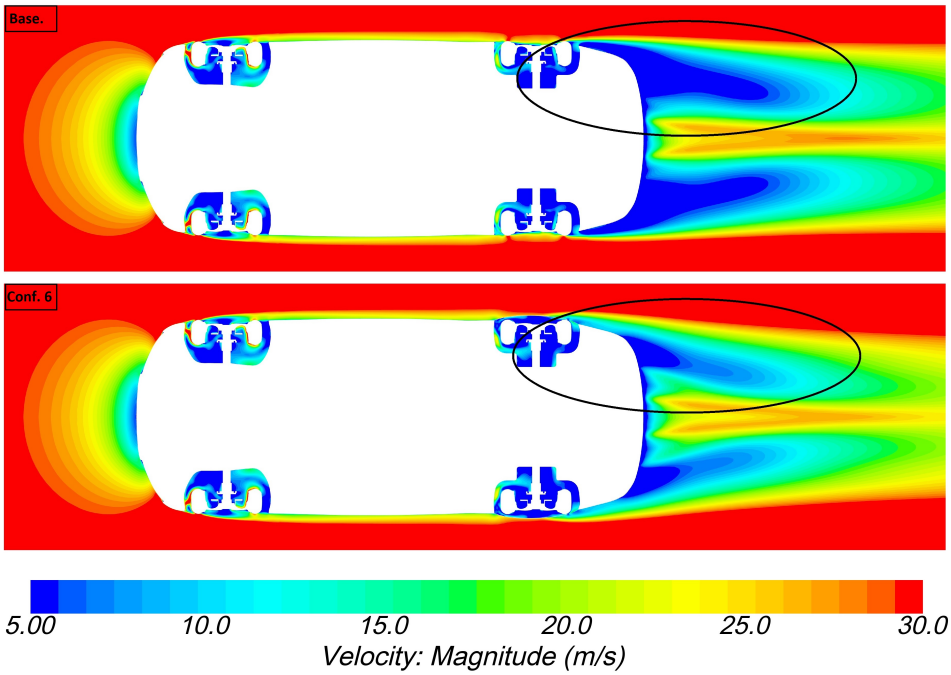

Figure 4.20: Velocity magnitude in x-y plane of the wheel center

At Base model, side of wheel is exposed to free flow directly and fluid decelerates due to hitting the wheel and causes a decrease at dynamic pressure, increases the static pressure. when using wheelhouse cover, the covers act as shield for wheel sides. So the flow does not affect wheel directly. Around the wheel surrounding, flow is slower and dynamic pressure is lower comparing with Base model. Thus, the static pressure does not increase as much as the Base model's. That is why drag reduction is observed at wheels with wheelhouse cover configurations (see Figure 4.21 - 4.26).

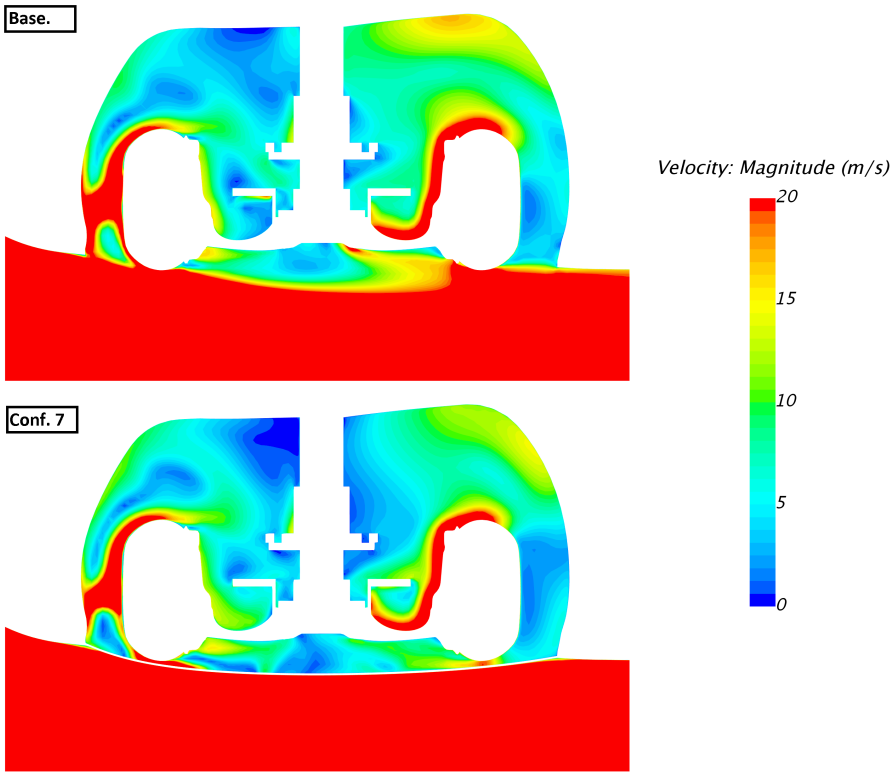

Figure 4.21: Velocity magnitude in x-y plane of the front wheel center for Base model and Configuration 7

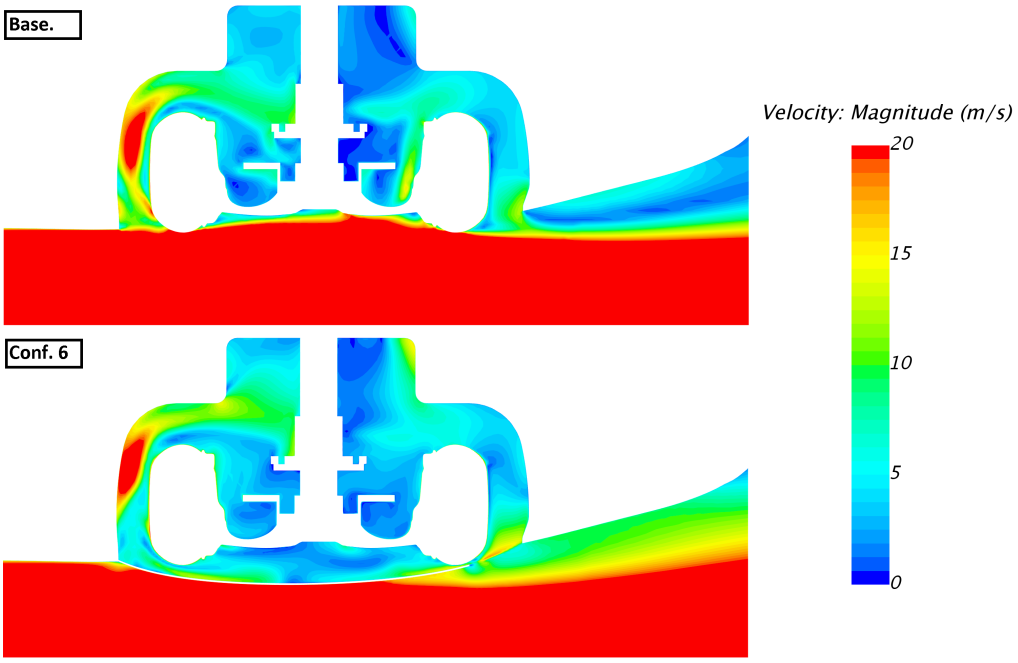

Figure 4.22: Velocity magnitude in x-y plane of the front wheel center for Base model and Configuration 6

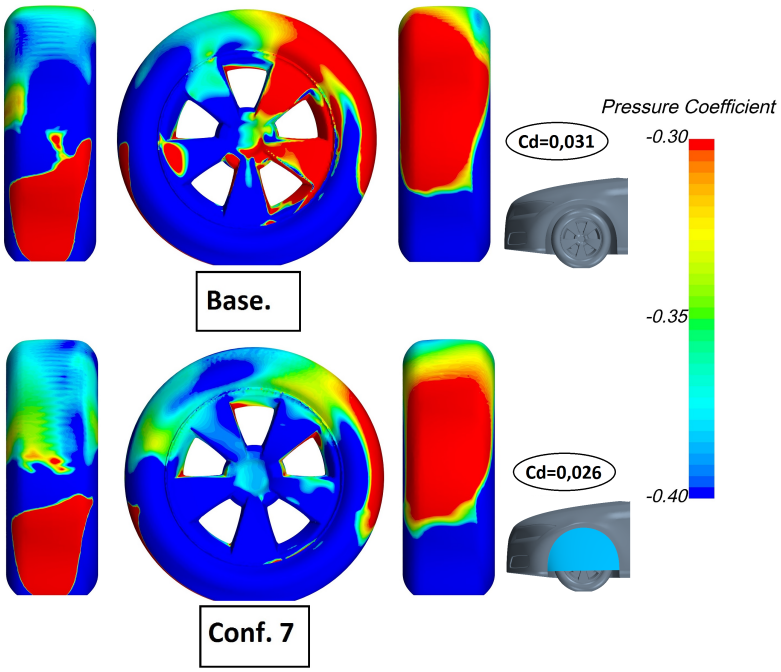

Figure 4.23: Pressure distribution in the front wheels of Base model and Configuration 7, front, side and rear view respectively

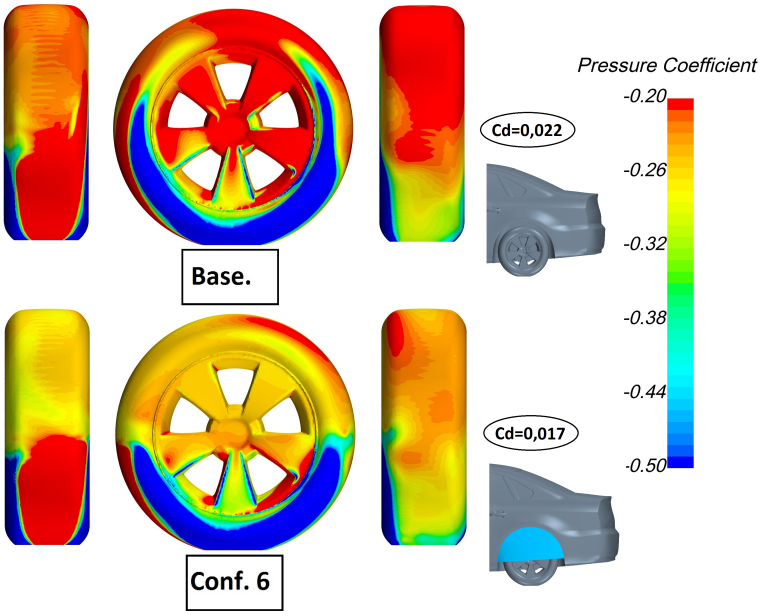

Figure 4.24: Pressure distribution in the rear wheels of Base model and Configuration 6, front, side and rear view respectively

In Figure 4.25, it is clearly visible that total pressure loss decreases around front wheel of Configuration 7. Which means that energy consumption decrease so that the drag also decrease in that area. Yet, according to Figure 4.26, total pressure loss increases at the center of rear wheel on Configuration 6 due to increase of frontal area. This may be the reason of Configuration 8 (front and rear wheelhouse covers)

has higher drag than Configuration 7. Drag may decrease if rear wheel cover is designed the way that does not affect frontal area.

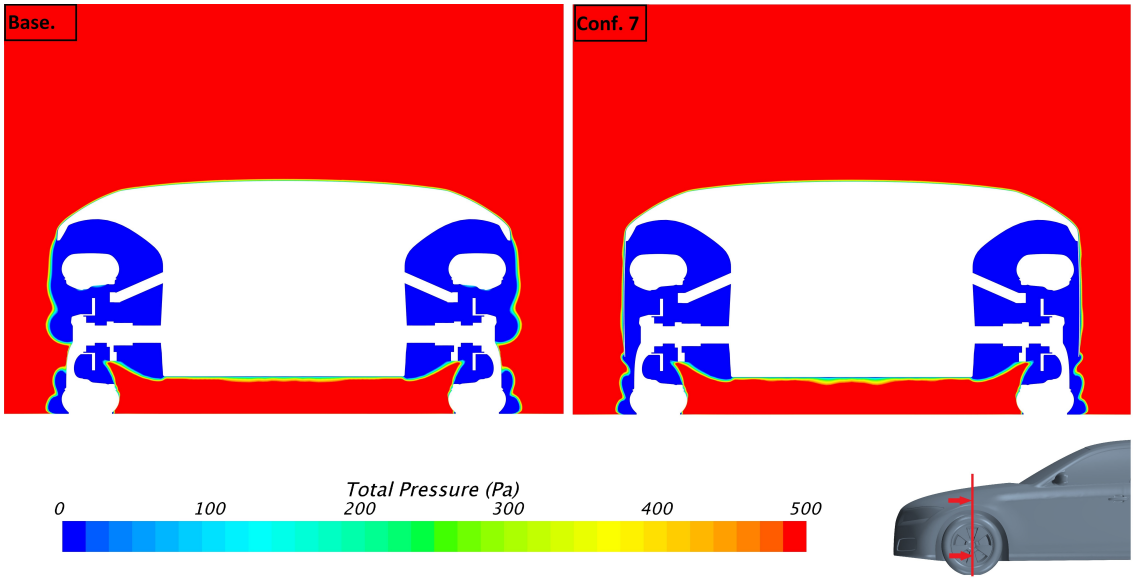

Figure 4.25: Total pressure distribution in y-z plane of the front wheel center

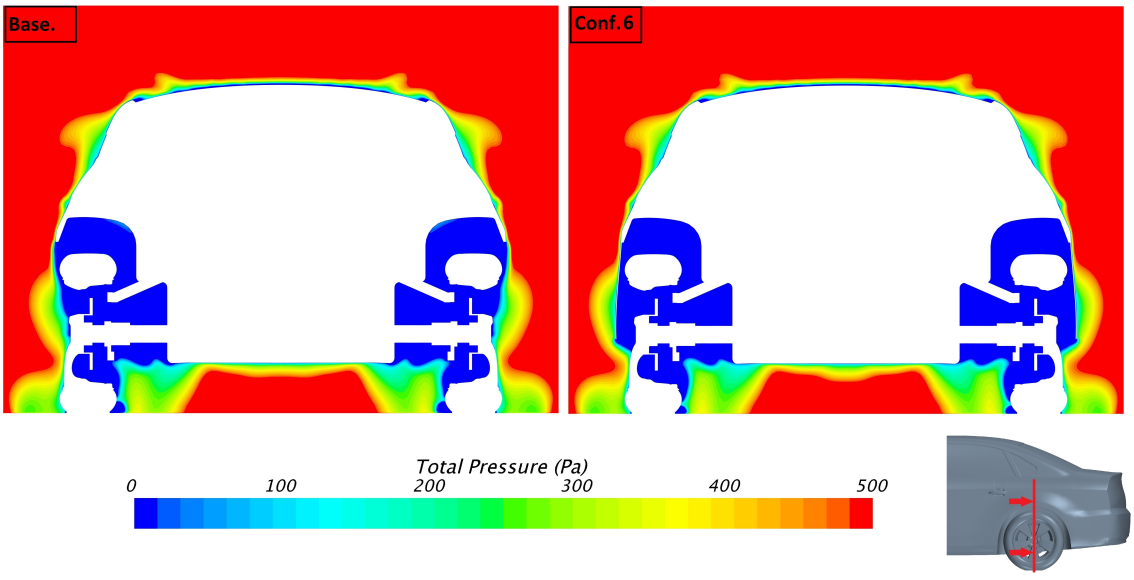

Figure 4.26: Total pressure distribution at y-z plane of the rear wheel center

4.4 The influence of rim design

4.4.1 Drag comparison

In Table 4.5, results of 8 different rim designs including Base model is shown. Minimum total drag is seen at Configuration 9 while maximum is seen at Configuration

14. According to previous studies [20, 17], covering the rim results in decrease of drag. Therefore this study expected to fully closed rim design will decrease the drag.Thus covering the rim from whether center or outer provides advantage. At fan type rim design drag coefficient is 9 counts more than Base model while at mirrored fan type is 2 counts lower. At Configuration 9 wheel drag reduction is higher than the others. Drag decreases 7 counts at front wheel and 4 counts at rear wheel. Despite the body drag increases, total drag is minimum since the drag reduction is high at wheels.

Table 4.5: C_D change with front wheel deflector height.

Configurations	Rims	Total Cd	Body Cd	Front Wheel	Rear wheel
(A) Base model	Base model	0,216	0,159	0,031	0,022
(B) Configuration 9	Fully closed	0,208	0,161	0,024	0,018
(C) Configuration 10	Inner covered (40mm gap thickness)	0,210	0,159	0,026	0,020
(D) Configuration 11	Inner covered (80mm gap thickness)	0,215	0,159	0,030	0,022
(E) Configuration 12	Outer covered design (40 mm gap thickness)	0,213	0,154	0,032	0,023
(F) Configuration 13	Outer covered (80 mm gap thickness)	0,212	0,157	0,03	0,021
(G) Configuration 14	Fan type	0,225	0,159	0,039	0,024
(H) Configuration 15	Mirrored fan type	0,214	0,161	0,029	0,022

4.4.2 The wheel drag comparison

In Figure 4.27 and Figure 4.28, total pressure distribution around the front wheels and the rear wheels are shown respectively. As it is understood from the figures, minimum pressure loss around wheel is at Configuration 9 while maximum is at Configuration 14. Decrease of total pressure shows non-reversible energy loss which means drag increases at that region. For this reason, while Configuration 9 with

minimum total pressure loss has the smallest C_D value (front wheel C_D=0.024, rear wheel C_D=0.018), Configuration-14 with maximum pressure loss has the greatest C_D value (front wheel C_D=0.039, rear wheel C_D=0,024). In brief, C_D reduction of front and rear wheels for Configuration 9 are 7 and 4 counts whereas C_D increment of front and rear wheels for Configuration 14 are 8 and 2 counts.

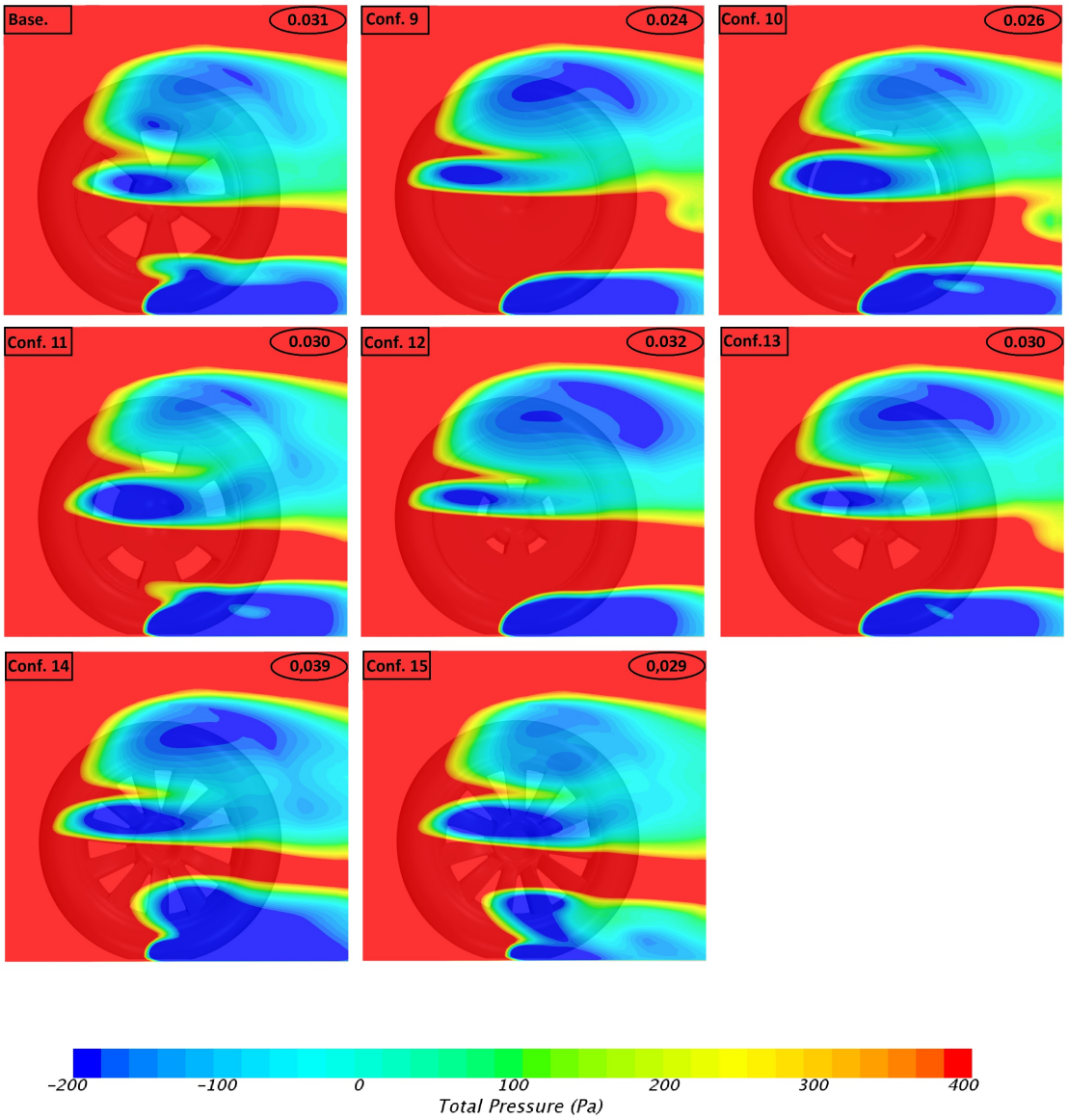

Figure 4.27: Total pressure distribution around the front wheels.

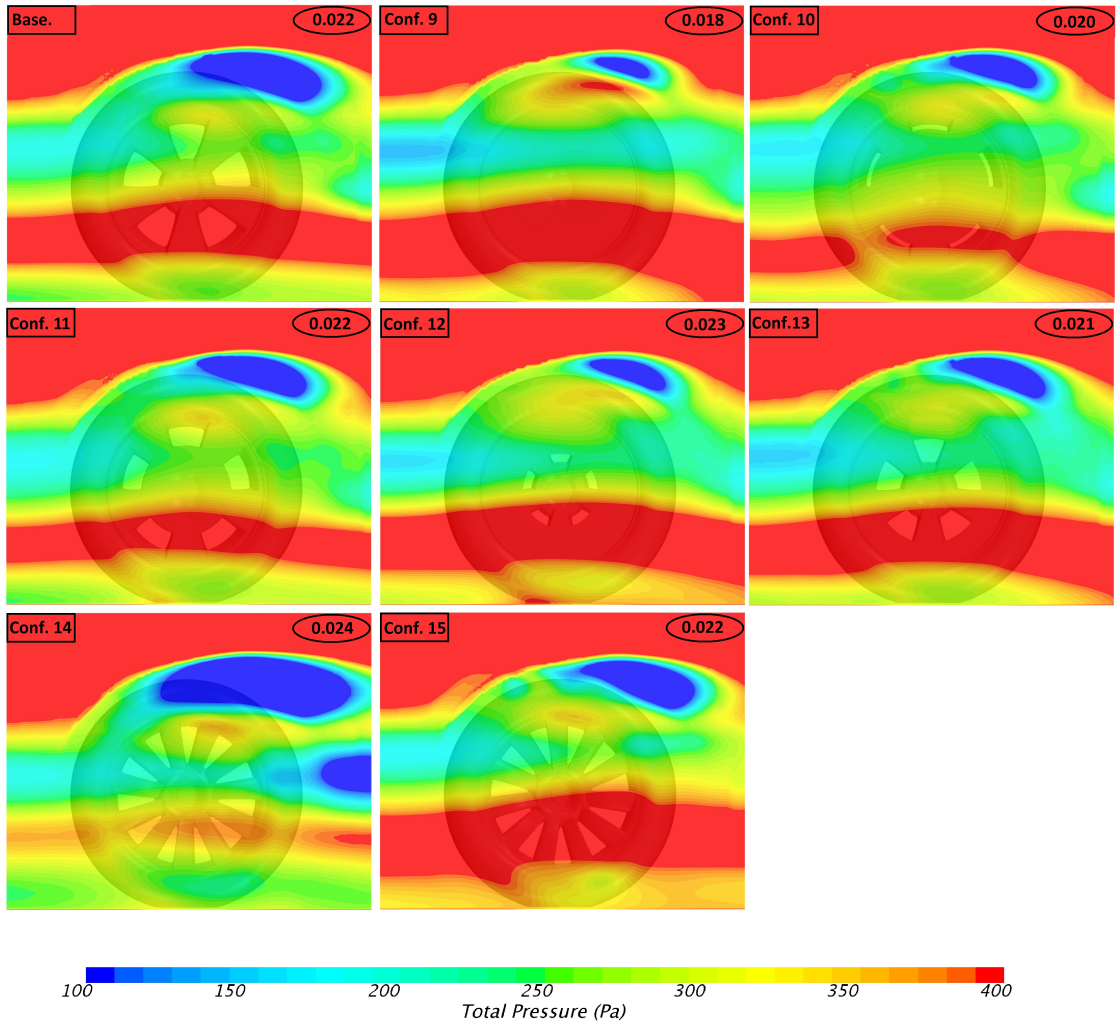

Figure 4.28: Total pressure distribution around the rear wheels.

4.4.3 Body drag

Figure 4.29 shows accumulated body C_D differences between Base model and Configuration 9 - Configuration 12. The accumulated C_D on Configuration 12, which gives minimum body C_D value, and Configurations 9, gives maximum C_D, were considered to show the effects of rim design on the body. At both Configurations, drag doesn't change before front wheel house. Then, from x = 0.35 m (starting wheel house) to center of front wheel, C_D at Configuration 9 decreases more than 2 counts and C_D of Configuration 12 decreases about 6 counts. In downstream of the front wheel centre, drag at Configuration 9 – 12 increases. After front wheel house, their C_D doesn't change until rear wheel house. At Configuration 9, C_D sharply increases more than 6 counts at upstream of the rear wheel center. Then, C_D decreases at downstream of the rear wheel center until back of car and body drag is 2 counts more than Base model.

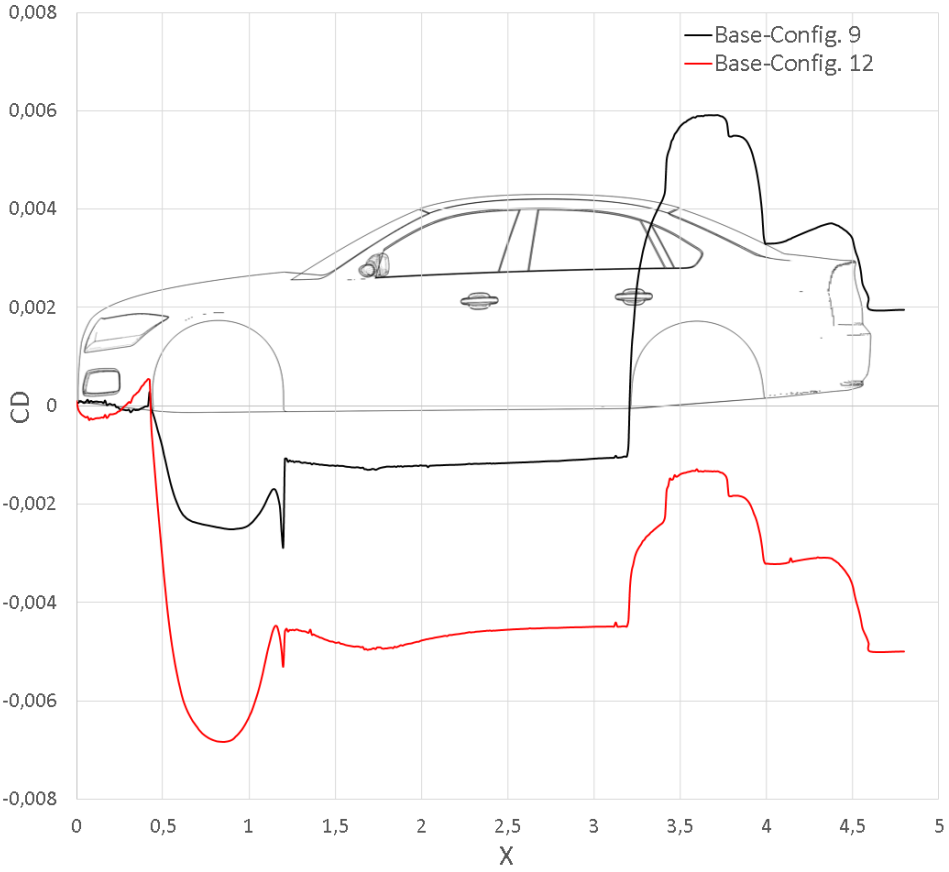

Figure 4.29: Accumulated body C_D distribution relative Base model Configuration 9 and Configuration 12.

In figure 4.30, pressure coefficient distribution inside front wheel houses for Base model and Configuration 12 are shown from sections inside front wheel houses (plane y=0.62). In front of the wheel house, velocity increased the parallel way through the surface at Base model. However in Configuration 12, verticality of velocity to surface and decrease at velocity while nearing the surface is observed at the same region. Hence flow nears through the surface and during nearing flow decelerates is deduced. As viscous effects are not dominant and the flow is incompressible, Bernoulli equation is valid. According to Bernoulli equations dynamic pressure of decelerated flow decreases while static pressure increases since the total pressure remains constant. This is the reason of increase at C_P value in here.

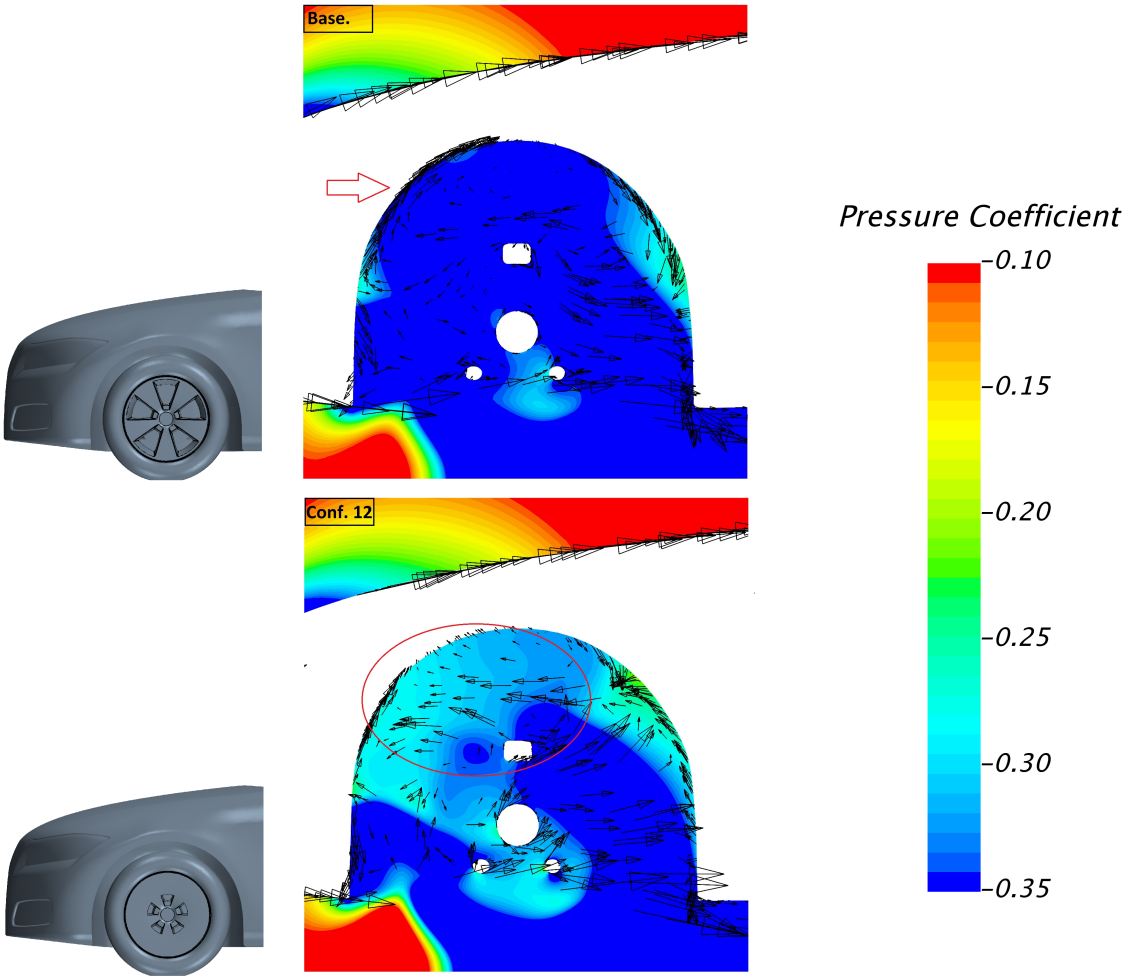

Figure 4.30: Pressure coefficient distribution inside front wheel houses for Base model and Configuration 12.

As shown earlier in Table 4.5, body C_D of Configuration 12 is 5 counts less than Base model. About 2 counts of this decrease are originated from the decline at back pressure (see Figure 4.29).Since changes at rims affect the flow inside the wheel house directly, accumulated drag changes along wheel houses due to varied rim designs. For this reason, in order to comprehend the effect of rim design along the car, streamlines colored with velocity magnitude exiting from both front and rear wheel house surfaces of Base model and Configuration 12 are given at Figure 4.29. It is obvious that Base wake width and dimension are smaller at Configuration 12 compared to Base model. This provides an increase at back pressure and decreases the body drag. (see Figure 4.32)

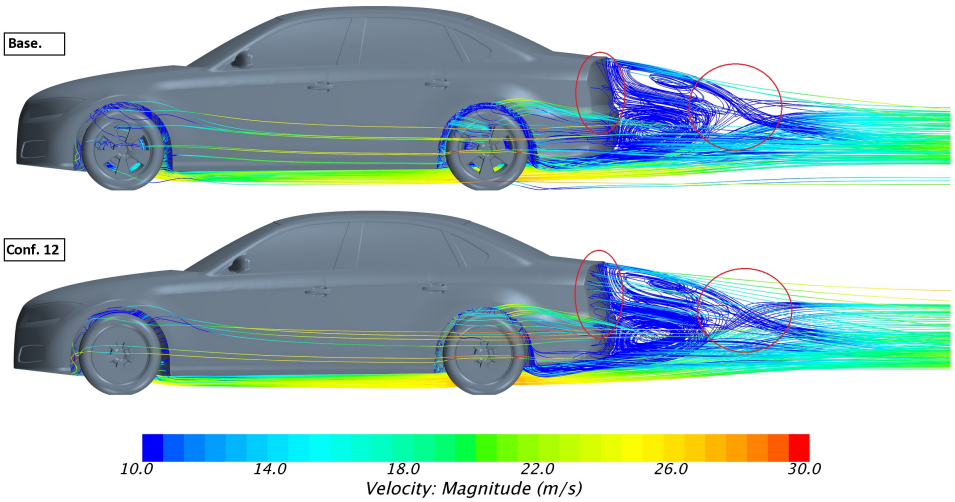

Figure 4.31: Streamlines colored according to velocity magnitude.

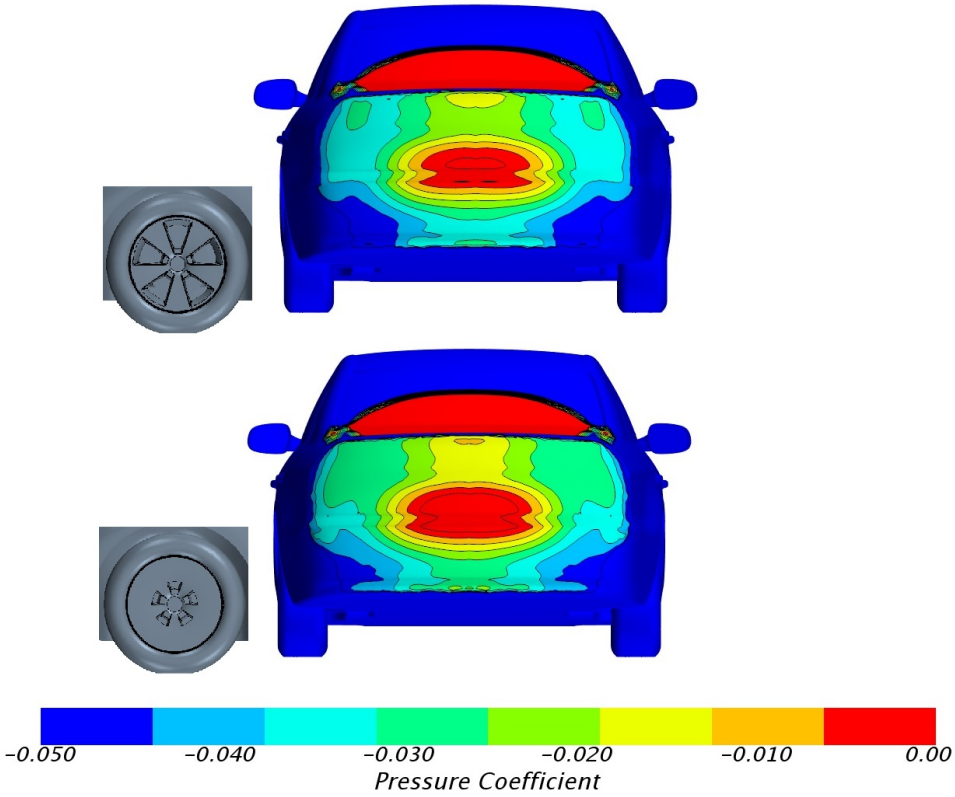

Figure 4.32: Base pressure measurements for Base model and Configuration 12.

5

Conclusion

The influence of the front deflector height on vehicle aerodynamic drag was investigated. 5 different configurations were simulated to find the optimum deflector height for drag reduction. The deflector heights that were simulated ranged between 20-60mm, in 10mm increments. It can be seen from the results that the drag reduces from 20 to 40 mm but then starts to increase thereafter. Thus 40mm height of the deflector is the most appropriate given the existing model of the car used. This configuration also gives the minimum body drag.

Of the three configurations simulated by modifying the wheel housing, it was seen that the configuration 7 (i.e. front wheel house covered) reduced total drag by 9 counts. The configuration 8 (i.e. both front and rear wheel house covered) reduced total drag by 8 counts. Contrary to the initial proposed hypothesis that the drag reduction of configuration 8 should be less than 7 because of both wheels being covered, we found that the simulations proved otherwise. This maybe partly because the introduction of the rear wheel housing increases the frontal surface area of the car body ?? increasing aerodynamic drag. If the rear wheel housing is to be redesigned in a better way so as to reduce the frontal surface area better performance of configuration 8 could be expected.

The effect of 7 different rim designs on vehicle aerodynamic drag were compared to the base rim design by numerical simulations. If we were to consider the total drag reduction then the configuration 9 is the best with 8 counts. The reduction mainly coming from the wheels with the front and rear wheels contributing to a count decrease of 7 and 4 respectively. This configuration though does increase the body count by 2. It is also interesting to see that the configuration 12 is the best, if we consider the drag reduction count contributed just by the body (C_D reduction is 5 counts). Of all the configurations, the configuration 14 is the worst with a drag increase of 9 counts.

These conclusions can only be applied on this specific vehicle. However, there is an indication that the same results might be shown with a similar type of vehicle.

6
Recommendation

If the same case is simulated with different sized computational grid and the results are unchanging, it can be inferred that the simulation is solved correctly. In addition, by providing enough resources, LES which is an unsteady solver, can be used. However, an unsteady solver cannot be used for the half model approach. Therefore, the whole model must be simulated in LES.

The effect of changing height of the deflector with constant width on drag is seen by the works done. Keeping the height constant with varied deflectors width can show the effect of deflector's width. Placing the deflector at different angles provide to see the position angle of deflector effect.

Covered wheel arc which closed only the gap between wheel and wheel house can be used for front and rear wheel separately and also all four wheelhouses closed simultaneously.

Configurations with different rim designs, front and rear wheel changed at the same time. Furthermore, front and rear wheel rims may be changed separately to observe the effect of total drag.

In addition, all results that are calculated with the computer models can be verified by wind tunnel test which gives more realistic results.

Bibliography

[1] *wikipedia/Aerodynamic drag*

[2] Hucho W.H., *Aerodynamics of Road Vehicles* 1998.

[3] M. Pfadenhauer, G. Wickern and K. Zwicker, *On the influence of wheels and tyres on the aerodynamic drag of the vehicles* 1996.

[4] A. Wäschle *The Influence of Rotating Wheels on Vehicle Aerodynamics - Numerical and Experimental Investigations* 2007.

[5] P. Elofsson and M. Bannister, *Drag Reduction Mechanisms Due to Moving Ground and Wheel Rotation in Passenger Cars,* 2002.

[6] E. Mercker, N. Breuer, H. Berneburg and H. J. Emmelmann, *On the Aerodynamic Influence Due to Rotating Wheels of Passenger Cars,* 1991.

[7] Emmanuelle Thivolle-Cazat, Patrick Gilliéron *Flow analysis around a rotating wheel* June, 2006

[8] Simone Sebben *Numerical Simulations of a Car Underbody: Effect of Front - Wheel Deflectors* March, 2004

[9] *How to Draw a Saab 9-3* https://i.ytimg.com/vi/4mo7CdT7biY/maxresdefault.jpg

[10] *NEVS Launches New Trademark - myAutoWorld.com* 2016-06-21.

[11] *saabsunited.com: NEVS to deliver 150,000 EV's to Panda New Energy Ltd.*

[12] *https://electrek.co/2017/03/01/chinese-battery-maker-catl-nevs-gigafactory/*

[13] Davidsson, Lars. *Mechanics of fluids. Part 2: Fluid dynamics and turbulence.* 2017.

[14] Nguyen, Cuong *Turbulence Modeling* November, 2005

[15] Star CCM+ 11.06 User's Guide; 2016

[16] ANSYS Fluent 12.0 Theory Guide; 2009

[17] Johan Cederlund, Jacob Vikström *The Aerodynamic Influence of Rim Design on a Sports Car and its Interaction with the Wing and Diffuser Flow* 2010.

[18] Frank M. White. *Fluid mechanics Sixth Edition. McGraw-Hill International Edition,* 2008.

[19] Reynolds, Osborne, *On the Dynamical Theory of Incompressible Viscous Fluids and the Determination of the Criterion* 1895.

[20] Alexey Vdovin *Investigation of Aerodynamic Resistance of Rotating Wheels on Passenger Cars* 2013.

[21] Q. Jia, M. M. Rashidi, SB. Ju, ZG. Yang *The Influence Of Wheel Spoiler Height on Vehicle Drag Reduction* September, 2015

[22] Wilcox, D.C. *Turbulence Modeling for CFD. 3rd edition.La Canada CA: DCW Industries* 2006.

[23] Menter, F.R. *F.R. Zonal two-equation k-ω turbulence model for aerodynamic flows* 1993.

[24] Wickern G., Zwicker K. and Pfadenhauer M., *Rotating Wheels – Their Impact on Wind Tunnel Test Techniques on Vehicle Drag Results* 1997.